The Astrophysical Journal, 733:60 (14pp), 2011 May 20 doi:10.1088/0004-637X/733/1/60

ACCRETION RATE AND THE PHYSICAL NATURE OF UNOBSCURED ACTIVE GALAXIES*

Jonathan R. Trump[1], Christopher D. Impey[1], Brandon C. Kelly[2,12], Francesca Civano[2], Jared M. Gabor[1], Aleksandar M. Diamond-Stanic[1], Andrea Merloni[3], C. Megan Urry[4], Heng Hao[2], Knud Jahnke[5], Tohru Nagao[6], Yoshi Taniguchi[6], Anton M. Koekemoer[7], Giorgio Lanzuisi[2], Charles Liu[8,9], Vincenzo Mainieri[10], Mara Salvato[3], and Nick Z. Scoville[11]
[1] Steward Observatory, University of Arizona, 933 North Cherry Avenue, Tucson, AZ 85721, USA
[2] Harvard-Smithsonian Center for Astrophysics, 60 Garden Street, Cambridge, MA 02138, USA
[3] Max-Planck-Institut für Extraterrestrische Physik, Giessenbachstrasse 1, D-85748 Garching, Germany
[4] Physics Department and Yale Center for Astronomy and Astrophysics, Yale University, New Haven, CT 06511, USA
[5] Max-Planck-Institut für Astronomie, Königstuhl 17, D-69117 Heidelberg, Germany
[6] Research Center for Space and Cosmic Evolution, Ehime University, 2-5 Bunkyo-cho, Matsuyama 790-8577, Japan
[7] Space Telescope Science Institute, 3700 San Martin Drive, Baltimore, MD 21218, USA
[8] Astrophysical Observatory, Department of Engineering Science and Physics, City University of New York, College of Staten Island, 2800 Victory Blvd., Staten Island, NY 10314, USA
[9] Hayden Planetarium, American Museum of Natural History, Central Park West at 79th Street, New York, NY 10024, USA
[10] European Southern Observatory, Karl-Schwarschild-Strasse 2, D-85748 Garching, Germany
[11] California Institute of Technology, MC 105-24, 1200 East California Boulevard, Pasadena, CA 91125, USA
Received 2010 July 8; accepted 2011 March 2; published 2011 May 5

ABSTRACT

We show how accretion rate governs the physical properties of a sample of unobscured broad-line, narrow-line, and lineless active galactic nuclei (AGNs). We avoid the systematic errors plaguing previous studies of AGN accretion rates by using accurate intrinsic accretion luminosities ($L_{\rm int}$) from well-sampled multiwavelength spectral energy distributions from the Cosmic Evolution Survey, and accurate black hole masses derived from virial scaling relations (for broad-line AGNs) or host–AGN relations (for narrow-line and lineless AGNs). In general, broad emission lines are present only at the highest accretion rates ($L_{\rm int}/L_{\rm Edd} > 10^{-2}$), and these rapidly accreting AGNs are observed as broad-line AGNs or possibly as obscured narrow-line AGNs. Narrow-line and lineless AGNs at lower specific accretion rates ($L_{\rm int}/L_{\rm Edd} < 10^{-2}$) are unobscured and yet lack a broad-line region. The disappearance of the broad emission lines is caused by an expanding radiatively inefficient accretion flow (RIAF) at the inner radius of the accretion disk. The presence of the RIAF also drives $L_{\rm int}/L_{\rm Edd} < 10^{-2}$ narrow-line and lineless AGNs to have ratios of radio-to-optical/UV emission that are 10 times higher than $L_{\rm int}/L_{\rm Edd} > 10^{-2}$ broad-line AGNs, since the unbound nature of the RIAF means it is easier to form a radio outflow. The IR torus signature also tends to become weaker or disappear from $L_{\rm int}/L_{\rm Edd} < 10^{-2}$ AGNs, although there may be additional mid-IR synchrotron emission associated with the RIAF. Together, these results suggest that specific accretion rate is an important physical "axis" of AGN unification, as described by a simple model.

Key words: accretion, accretion disks – galaxies: active – galaxies: nuclei – galaxies: Seyfert – quasars: emission lines – quasars: general

Online-only material: color figures, machine-readable table

1. INTRODUCTION

Supermassive black holes (SMBHs) are now known to be ubiquitous in the centers of all massive galaxies (Magorrian et al. 1998). SMBHs grow in an "active" phase of accretion, during which they are observed as active galactic nuclei (AGNs). AGN growth is intimately tied to galaxy evolution, as evident in the well studied correlations between SMBH mass ($M_{\rm BH}$) and properties of the host galaxy bulge (e.g., Gebhardt et al. 2000; Ferrarese & Merritt 2000; Marconi & Hunt 2003). The AGN phase is also hypothesized to regulate star formation in its host galaxy, with the galaxy feeding the black hole in turn (e.g., Di Matteo et al. 2005; Younger et al. 2008). All massive galaxies are thought to experience episodic AGN behavior in their lifetimes (Soltan 1982; Marconi et al. 2004).

AGNs are generally classified by differences in their optical spectra. Type 1 or broad-line AGNs have broad ($v_{\rm FWHM} \gtrsim 1000$ km s^{-1}) emission lines superimposed on blue unobscured continua in the UV/optical (e.g., Vanden Berk et al. 2001), and are the most luminous persistent sources in the sky. Type 2 or narrow-line AGNs lack broad emission lines and have weaker continua (frequently dominated by their host galaxies), but have strong narrow emission lines, especially from forbidden transitions. Narrow emission lines associated with nuclear activity can be distinguished from lines caused by star formation by studying the line ratios (Baldwin et al. 1981). The line ratio diagnostics work because the "harder" emission of an AGN is more efficient at ionizing the surrounding gas and dust than star formation, and thus AGNs have stronger lines from high-energy forbidden transitions (e.g., O III λ5007 and N II λ6583) relative to the lower-energy hydrogen transitions (e.g., Hβ λ4861 and Hα λ6563). The subclass of "low-ionization nuclear emission region" AGNs (LINERs; Heckman 1980)

* Based on observations with the *XMM-Newton* satellite, an ESA science mission with instruments and contributions directly funded by ESA member states and NASA; the Magellan telescope, operated by the Carnegie Observatories; the ESO Very Large Telescope; and the MMT Observatory, a joint facility of the University of Arizona and the Smithsonian Institution; the Subaru Telescope, operated by the National Astronomical Observatory of Japan; and the NASA/ESA *Hubble Space Telescope*, operated at the Space Telescope Science Institute, which is operated by AURA Inc., under NASA contract NAS 5-26555.
[12] Hubble Fellow.

have narrow emission lines that are probably excited by some combination of ionization from both star formation and an AGN (Eracleous et al. 2010). Deep X-ray surveys have additionally revealed "optically dull" AGNs (Elvis et al. 1981; Comastri et al. 2002), which have bright X-ray emission but none of the broad or narrow emission line signatures of AGN accretion. While many optically dull AGNs can be explained as Type 2 AGNs diluted by prominent host galaxies (Moran et al. 2002; Caccianiga et al. 2007), at least $\sim$1/3 are undiluted but intrinsically optically weaker than other AGNs (Trump et al. 2009c). The inferred X-ray column density $N_{\rm H}$ can also be used to classify AGNs, with Type 2 (narrow-line) AGNs typically more X-ray absorbed than Type 1 (broad-line) AGNs. However, X-ray and optical classifications differ for $\sim$20% of objects (Trouille et al. 2009).

Historically, Type 2 and optically dull AGNs have been described as obscured versions of Type 1 AGNs, with the broad emission line region (BLR) hidden behind a partially opaque "torus" of gas and dust, while the narrow emission lines lie outside the torus (e.g., Krolik & Begelman 1988). The best evidence for this scenario is the observation that some Type 2 AGNs have a "hidden" BLR revealed by spectropolarimetry (Antonucci 1993). However, recent observations have revealed several serious limitations of a simple unified model based solely on geometric obscuration. Even in very deep spectropolarimetric observations, many Type 2 AGNs show no hidden BLR (Barth et al. 1999; Tran 2001; Wang & Zhang 2007). Observations suggest a lower $L/L_{\rm Edd} \geqslant 0.01$ limit in accretion rate for broad-line AGNs (Kollmeier et al. 2006; Trump et al. 2009b), although they remain incomplete at low accretion rates and low masses (Kelly et al. 2010). The X-ray spectra are unabsorbed ($N_{\rm H} \lesssim 10^{21}$ cm^{-2}) for 30%–40% of Type 2 AGNs (Mainieri et al. 2007; Trouille et al. 2009) as well as most local LINERs (Ho 2008, and references therein) and distant optically dull AGNs (Trump et al. 2009c). Several well studied LINERs additionally lack the narrow Fe Kα emission signature of a dusty torus (Ptak et al. 2004; Bianchi et al. 2008). Many Type 2 AGNs and most optically dull AGNs have mid-IR colors like normal galaxies (Ho 2008; Trump et al. 2009c), in contrast to the hot mid-IR colors of Type 1 AGNs described by torus models (Nenkova et al. 2008; Mor et al. 2009). Toroidal obscuration is additionally ruled out for some strongly varying Type 2 (Hawkins 2004) and optically dull AGNs (Trump et al. 2009c) since these objects have continua that vary on year timescales, well within the inferred light-travel time dimension of any torus.

Several authors have proposed models that use different accretion rates as a cause of the differences between observed AGNs. Elitzur & Ho (2009) suggest that the BLR and "torus" are inner (ionized) and outer (clumpy and dusty) parts of the same disk-driven wind and that this wind is no longer supported at low accretion rates (see also Elitzur & Shlosman 2006; Nenkova et al. 2008). Similarly, Nicastro (2000) suggested that low accretion rates actually drive the disk wind within the last stable orbit of the SMBH, meaning that the BLR cannot form. Models for radiatively inefficient accretion (e.g., Yuan 2007) suggest that at $L/L_{\rm Edd} \lesssim 10^{-2}$ the accretion disk becomes truncated near the SMBH, with a geometrically thick and optically thin disk at lower radii, and a normal thin disk (e.g., Shakura & Sunyaev 1973) at higher radii. Such objects are predicted to lack strong emission lines (both broad and narrow) and have weak UV/optical emission, as observed in many optically weak low-luminosity AGNs (Ho 2009) and X-ray bright, optically dull AGNs (Trump et al. 2009c). Hopkins et al. (2009) additionally show that X-ray hardness, generally attributed to X-ray absorption, may also result from the naturally X-ray hard spectrum expected from radiatively inefficient accretion.

In this work, we directly measure Eddington ratios for a large, X-ray-selected sample of broad-line, narrow-line, and lineless AGNs. The Eddington ratio is a unitless measure of accretion power, defined as $\lambda \equiv L_{\rm int}/L_{\rm Edd}$ (with $L_{\rm int}$ being the intrinsic accretion luminosity). The sample is drawn from the Cosmic Evolution Survey (COSMOS; Scoville et al. 2007) X-ray AGN sample (Trump et al. 2007), as described in Section 2. Estimates of specific accretion rates are described in Section 3, with intrinsic accretion luminosity measured directly from fits to the multiwavelength continuum (avoiding uncertain bolometric corrections) and black hole masses from the broad-line scaling relations (for broad-line AGNs) or the $M_{\rm BH}$–M_* relations (for narrow-line and lineless AGNs). In Section 4, we show that broad emission lines are present only at high accretion rates ($L_{\rm int}/L_{\rm Edd} > 0.01$), while narrow-line and lineless AGNs at lower accretion rates have cooler disks, stronger radio jets, and no torus IR signature. We present a "cartoon" model which summarizes our results in Section 5, with predictions for future observations in Section 6. We adopt a cosmology with $h = 0.70$, $\Omega_M = 0.3$, and $\Omega_\Lambda = 0.7$ throughout.

2. OBSERVATIONAL DATA

Measuring an accurate specific accretion rate requires accurate accretion luminosities and black hole mass estimates. In particular, spectral energy distribution (SED) measurements from optical/UV to X-ray are necessary to constrain intrinsic luminosities to within a factor of a few (as we show in Section 3.1). We select a sample of 348 AGNs from the COSMOS (Scoville et al. 2007) field, which is based on the 1.7 deg^2 *Hubble Space Telescope* (*HST*)/Advanced Camera for Surveys (ACS) mosaic (Koekemoer et al. 2007). These AGNs have multiwavelength data in the form of *Spitzer*/IRAC, *HST*/ACS, Subaru/Suprime-Cam, *GALEX*, *XMM-Newton*, and *Chandra* observations, as described in Table 1. Spectroscopic identification and redshifts for these objects come from archival Sloan Digital Sky Survey (SDSS) data, Magellan/IMACS and MMT/Hectospec (Trump et al. 2009a), and Very Large Telescope (VLT)/VIMOS observations (Lilly et al. 2007).

The sample is selected from the parent catalog of 1651 *XMM*-COSMOS point sources with optical counterparts (Brusa et al. 2010), limited by $f_{0.5-2\,{\rm keV}} > 2 \times 10^{-16}$ erg s^{-1} cm^{-2}. Of these X-ray point sources, 649 objects with $i_{\rm AB} < 23.5$ have high-confidence (>90% likelihood as correct) identifications and redshifts from optical spectroscopy (Trump et al. 2009a; Lilly et al. 2007) in COSMOS. Most of the X-ray point sources without spectroscopy were missed simply due to random slit placement constraints. The optical spectroscopy is $\sim$90% complete to $i_{\rm AB} < 22.5$, although the completeness is redshift dependent. For broad-line AGNs, the spectroscopic completeness is lower at $0.5 < z < 1$, $z \sim 1.4$, and $z \sim 2.4$, especially at $i_{\rm AB} > 22.5$ (see Figure 13 of Trump et al. 2009a). For narrow-line and lineless AGNs, spectroscopic completeness drops dramatically at $z > 1.2$, since at higher redshifts the 4000 Å break and the O II feature shift redward of the observed wavelength range. To ensure that X-ray objects with narrow-line and lineless spectra are bona fide AGNs, we select only objects with $L_{0.5-10\,{\rm keV}} > 3 \times 10^{42}$ erg s^{-1}. This X-ray luminosity limit is generally used to separate AGNs from X-ray fainter starburst galaxies (e.g., Hornschemeier et al. 2001). We also include

Table 1
COSMOS Multiwavelength Data

Band	Telescope	Wavelength (Å)	Energy (eV)	Limit (AB mag)[b]	NL/LL AGNs Detected	BL AGNs Detected	Reference[a]
$X_{\rm hard}$	*Chandra*	1.24–6.20	2000–10000	7.3×10^{-16}	79/92	228/256	(1)
$X_{\rm hard}$	*XMM*	1.24–6.20	2000–10000	9.3×10^{-15}	79/92	228/256	(2)
$X_{\rm soft}$	*Chandra*	6.20–24.8	500–2000	1.9×10^{-16}	88/92	249/256	(1)
$X_{\rm soft}$	*XMM*	6.20–24.8	500–2000	1.7×10^{-15}	88/92	249/256	(2)
FUV	*GALEX*	1426–1667	7.44–8.63	25.7	27/92	131/256	(3)
NUV	*GALEX*	1912–2701	4.59–6.84	26.0	55/92	184/256	(3)
u^*	CFHT	3642–4180	2.97–3.40	26.4	92/92	254/256	(4)
B_J	Subaru	4036–4843	2.56–3.07	27.7	92/92	256/256	(4)
g^+	Subaru	4347–5310	2.33–2.85	27.1	92/92	256/256	(4)
V_J	Subaru	4982–5916	2.10–2.49	27.0	92/92	255/256	(4)
r^+	Subaru	5557–6906	1.80–2.23	27.1	92/92	256/256	(4)
i^*	CFHT	6140–9119	1.36–2.02	26.7	92/92	256/256	(4)
F814W	*HST*/ACS	7010–8880	1.40–1.77	27.2	92/92	256/256	(5)
z^+	Subaru	8544–9499	1.31–1.45	25.7	92/92	254/256	(4)
J	UKIRT	11665–13223	0.94–1.06	23.8	92/92	256/256	(4)
Ks	CFHT	19900–23050	0.538–0.623	23.4	92/92	253/256	(6)
IRAC1	*Spitzer*	31557–38969	0.318–0.383	23.9	91/92	255/256	(4)
IRAC2	*Spitzer*	39550–49663	0.250–0.313	23.3	91/92	255/256	(4)
IRAC3	*Spitzer*	50015–63514	0.195–0.248	21.3	91/92	255/256	(4)
IRAC4	*Spitzer*	62832–91229	0.136–0.197	21.0	91/92	255/256	(4)
1.4 GHz	VLA	2×10^9	6×10^{-6}	20 μJy	92/92	256/256	(7)

Notes.
[a] References are as follows: (1) Elvis et al. 2009; (2) Cappelluti et al. 2009; (3) Zamojski et al. 2007; (4) Ilbert et al. 2009; (5) Koekemoer et al. 2007; (6) McCracken et al. 2010; (7) Schinnerer et al. 2007.
[b] X-ray flux limits are given in erg s^{-1} cm^{-2}, and the radio flux limit is given in μJy.

seven broad-line AGNs without X-ray detection, six of which were selected by their *Spitzer*/IRAC colors and one which is a serendipitous object from the bright zCOSMOS survey (which selected targets based only on $i_{\rm AB} < 22.5$). While these seven X-ray-undetected AGNs do not come from a complete sample, we include them to gain a larger parameter space of AGN spectral types and accretion rates (in effect, when using their X-ray limits, they occupy the same $L_{\rm disk}/L_X$ parameter space as a few other X-ray-detected AGNs). Restricting narrow-line and lineless AGNs to be X-ray luminous and adding the seven X-ray-undetected broad-line AGNs make a parent sample of 380 broad-line, 124 narrow-line, and 49 lineless AGNs (553 total) with high-confidence redshifts and spectral identification.

Measuring accurate black hole masses further constrains the sample to certain redshift ranges. For Type 1 AGNs, we require the presence of one of the C IV, Mg II, or Hβ broad emission lines in the observed spectral range, effectively limiting broad-line AGNs with IMACS or VIMOS spectra to $0.16 < z < 0.88$, $1 < z < 2.4$, and $2.7 < z < 4.9$, and objects with Hectospec or SDSS spectra to $z < 4.9$. For narrow-line and lineless AGNs, we estimate black hole mass from the $M_{\rm BH}$–$L_{\rm bulge}$ relation, and so we require an accurate estimate of $L_{\rm bulge}$. For this we use the sample of objects in COSMOS with morphological decompositions (Gabor et al. 2009) from the *HST*/ACS images (Koekemoer et al. 2007), which also effectively limits the narrow-line and lineless AGNs to $z < 1.2$ (beyond which the 4000 Å break shifts out of the ACS-*i* band and the host galaxy is much more difficult to detect). The accurate host measurements from Gabor et al. (2009) additionally allow us to subtract the host component before computing the intrinsic bolometric luminosity. In general, the narrow-line and lineless AGNs are biased toward lower redshift and consequently higher mass, since AGNs grow over cosmic time. The narrow-line and lineless AGNs have a mean redshift of 0.7, while the broad-line AGNs have a mean redshift of 1.6. The final sample of 348 AGNs includes 256 broad-line, 65 narrow-line, and 27 lineless AGNs.

Full multiwavelength data exist for >95% of the AGNs in the sample in every wavelength region except the UV. X-ray data exist from both *Chandra* and *XMM-Newton*: we use the deeper *Chandra* data when available, but the *Chandra* observations cover only the central 0.8 deg^2 of the COSMOS field. For the seven X-ray-undetected broad-line AGNs, we use the 0.5–2 keV *XMM* flux limit ($f_{0.5-2\,\rm keV} = 2 \times 10^{-16}$ erg s^{-1} cm^{-2}) for their X-ray luminosity (since these AGNs have $L_{\rm disk}/L_X > 10$, their bolometric luminosity is dominated by their optical/UV emission, and completely neglecting their X-ray emission does not significantly change their bolometric luminosity estimate). We apply the zero-point offsets derived by Ilbert et al. (2009) to the IR–UV photometry.

2.1. Measuring Absorption and Extinction

X-ray absorption and optical/UV extinction could pose a challenge to measuring the intrinsic accretion power. The most heavily absorbed AGNs (e.g., Compton-thick AGNs with $N_{\rm H} > 10^{24}$ cm^{-2}) are entirely missed by our survey because they lack detectable X-ray emission (e.g., Treister et al. 2004). But if an AGN is moderately absorbed and still X-ray detected, we might expect its disk to appear cooler because the UV light is preferentially extincted and its X-ray slope to appear harder because the soft X-rays are preferentially absorbed. Some AGNs are also intrinsically reddened, decreasing their UV emission by a factor of two to three (Richards et al. 2003) and causing us to underestimate their accretion disk emission. With absorbed soft X-rays and extincted disk emission, we could significantly underestimate $L_{\rm int}/L_{\rm Edd}$.

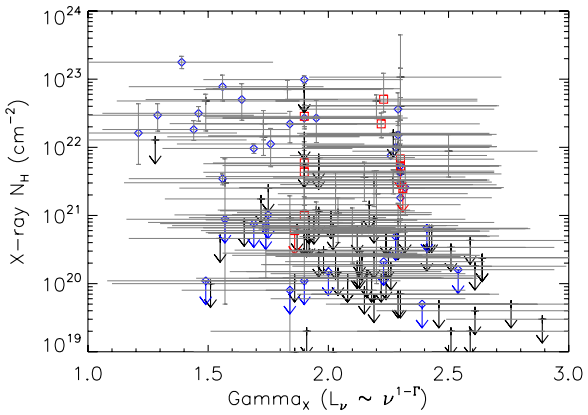

Figure 1. Column density $N_{\rm H}$ and the X-ray slope Γ_X measured from the X-ray spectrum for the 153 AGNs with >40 *XMM* or *Chandra* counts. X-ray slope Γ_X is defined by $L_\nu \propto \nu^{1-\Gamma_X}$. Black crosses show broad-line AGNs, blue diamonds show narrow-line AGNs, and red squares show lineless (optically dull) AGNs. The median X-ray slope for all AGNs is $\Gamma_X = 2.1$, although Γ_X ranges from 1 to 3. There are 118 unobscured AGNs with $N_{\rm H} < 10^{22}$ cm^{-2}.

(A color version of this figure is available in the online journal.)

We use X-ray column density $N_{\rm H}$ to characterize the obscuration properties of our AGNs. Column density and optical extinction are roughly correlated, with $A_V/N_{\rm H} \sim 2 \times 10^{-23}$ cm^2 (Martinez-Sansigre et al. 2006). Then, at $N_{\rm H} < 10^{22}$ cm^{-2}, optical magnitude should be extincted by $\lesssim$20% ($\lesssim$0.2 mag). Assuming a Small Magellanic Cloud reddening law (Pei 1992), as is most appropriate for AGNs, this optical extinction translates to a factor of ~1.2 extinction at 3000 Å in the UV. Maiolino et al. (2001) showed that the A_V–$N_{\rm H}$ relation varies by up to a factor of 30 because of unknown changes in the gas-to-dust ratio, grain size, and/or different physical locations of the optical and X-ray absorbing material. However, for all AGNs in the Maiolino et al. (2001) sample with $L_X > 10^{42}$ erg s^{-1}, $A_V/N_{\rm H} < 1.8 \times 10^{-22}$ cm^2, meaning at $N_{\rm H} \sim 10^{22}$ cm^{-2} even the maximum optical (V-band) extinction is a factor of 5 and the maximum UV (3000 Å) extinction is a factor of 30.

Column density $N_{\rm H}$ can be accurately measured for the 153 AGNs (93 broad-line, 38 narrow-line, and 22 lineless AGNs) in the sample that have >40 *XMM* or *Chandra* counts. (With less than 40 counts, the spectral fitting does not always stably converge.) We fit each X-ray spectrum as an intrinsically absorbed power law with Galactic absorption ($N_{\rm H,gal} = 2.6 \times 10^{20}$ cm^2 in the direction of the COSMOS field), with the power-law slope and $N_{\rm H}$ as free parameters. The best-fit $N_{\rm H}$ value and its error are found using the Cash (1979) statistic. We present $N_{\rm H}$ and X-ray slope Γ in Figure 1. Among the 153 AGNs with >40 X-ray counts, there are 118 unobscured AGNs with $N_{\rm H} < 10^{22}$ cm^{-2} (82 broad-line, 24 narrow-line, and 12 lineless AGNs). We restrict our main conclusions to this set of 118 unobscured AGNs for the remainder of this work.

3. CHARACTERIZING THE AGN-SPECIFIC ACCRETION RATE

In this work, we describe the specific accretion rate using the Eddington ratio parameter $\lambda \equiv L_{\rm int}/L_{\rm Edd}$. Here, $L_{\rm int}$ is the intrinsic luminosity, a measure of the total accretion luminosity which includes only light from the accretion disk and X-ray corona and excludes any reprocessed IR emission. While the reprocessed IR emission can represent a large fraction of the bolometric luminosity, especially for obscured AGNs, it may be anisotropic. Most of our AGNs are unobscured (see Section 2.1) and we exclude the IR emission to avoid double counting the AGN emission. Instead we use only the optical/UV and X-ray emission that comes directly from the disk and corona in the AGN; in this work, when using "intrinsic" luminosity we are always referring to the total of the disk (optical/UV) and corona (X-ray) emission, without the reprocessed (IR) emission. The Eddington luminosity is derived from the black hole mass, with $L_{\rm Edd} = 1.3 \times 10^{38}\,(M_{\rm BH}/M_\odot)$ erg s^{-1}. AGN luminosity is powered by the accretion rate, with $L_{\rm int} = \eta \dot{M} c^2$. For a constant efficiency η, the Eddington ratio λ is equivalent to the specific accretion rate $\dot{m} \equiv \dot{M}/\dot{M}_{\rm Edd}$. For example, assuming $\eta \sim 0.1$ the Eddington accretion rate can be written as $\dot{M}_{\rm Edd} = 5 M_8\ M_\odot$ yr^{-1}, with $M_8 = M/(10^8 M_\odot)$. However, there is good evidence that η decreases at very low accretion rates $\dot{m} \ll 0.01$ (e.g., Narayan & McClintock 2008). Indeed, in Sections 4 and 5 we invoke a lower-efficiency (radiatively inefficient) accretion to explain the observational properties of $L_{\rm int}/L_{\rm Edd} < 10^{-2}$ AGNs. This means that the accretion power $L_{\rm int}/L_{\rm Edd}$ probably underestimates the accretion rate $\dot{m}$ for our most weakly accreting AGNs with $L_{\rm int}/L_{\rm Edd} < 10^{-2}$; for example, a measured accretion power of $L_{\rm int}/L_{\rm Edd} \sim 10^{-4}$ might correspond to $\dot{m} \sim 10^{-3}$.

Below, we outline our methods for estimating black hole masses and bolometric luminosities from the data for the AGNs in our sample. Table 2 presents the full catalog of $L_{\rm int}$, $M_{\rm BH}$, and $L_{\rm int}/L_{\rm Edd}$, and their associated errors, for our AGNs.

3.1. Intrinsic Luminosity Estimates

We calculate the intrinsic luminosity from the full rest-frame near-IR to X-ray multiwavelength data. This avoids monochromatic bolometric corrections which are highly uncertain and probably depend on the Eddington ratio (e.g., Kelly et al. 2008; Vasudevan & Fabian 2009). Instead, we measure intrinsic luminosity by integrating the best-fit accretion disk + X-ray power-law SED model. We compile the broadband near-IR (Ks, J), optical (z^+, r^+, i^*, g^+, V_J, B_J, u^*), UV (*GALEX* NUV and FUV), and X-ray (0.5–2 keV and 2–10 keV from *Chandra* when available or *XMM-Newton*) data, for which the wavebands and limits are described in Table 1. To avoid reprocessed mid-IR emission, which would double count the intrinsic emission for an unobscured AGN, we restrict the accretion disk fit to rest frame 1eV $< E <$ 100 eV (12,400 Å $> \lambda >$ 124 Å). The radio emission is negligible in the total energy output of our AGNs. While narrowband optical photometry also exists for our AGNs, its inclusion does not appreciably change the best-fit multiwavelength SED compared to using only the broadband data.

The rest-frame near-IR and optical emission of narrow-line and lineless AGNs is dominated by the emission from the host galaxy. For these objects, accurate intrinsic luminosities require modeling and subtracting the host galaxy light. Gabor et al. (2009) measured the host F814W luminosities from surface brightness fitting to the *HST*/ACS data of our AGNs. We use this luminosity to scale a galaxy template from Polletta et al. (2007). Lineless AGNs have early-type hosts, since their spectra lack the emission lines associated with a late-type star-forming galaxy, and so we use the "Ell5" early-type template from Polletta et al. (2007). The narrow-line galaxies in our sample typically have intermediate-type ("green valley") hosts based on their morphologies (Gabor et al. 2009) and star formation rates (Silverman et al. 2009), and so we use the "S0" template of Polletta et al. (2007). We subtract the host contribution in each photometric band before performing our SED fit. The reddest

Table 2
Catalog of AGNs

R.A.+Decl. (J2000) (hhmmss.ss+ddmmss.s)	Type[a]	Redshift	Spec.[b] Source	$L_{\rm int}$ $\log(\rm erg\,s^{-1})$	$M_{\rm BH}$ $\log(M_\odot)$	$\log(L_{\rm int}/L_{\rm Edd})$
095728.34+022542.2	BL	1.54	S	$46.03^{+0.52}_{-0.10}$	$8.40^{+0.36}_{-0.43}$	$-0.49^{+0.58}_{-0.27}$
095740.78+020207.9	BL	1.48	I	$45.88^{+0.64}_{-0.30}$	$8.24^{+0.45}_{-0.39}$	$-0.47^{+0.68}_{-0.40}$
095743.33+024823.8	BL	1.36	S	$45.84^{+0.66}_{-0.16}$	$8.24^{+0.44}_{-0.36}$	$-0.51^{+0.18}_{-0.66}$
095749.02+015310.1	NL	0.32	I	$43.89^{+0.71}_{-0.21}$	$8.61^{+0.29}_{-0.30}$	$-2.84^{+0.73}_{-0.15}$
095750.20+022548.3	BL	1.24	Z	$44.93^{+0.52}_{-0.20}$	$7.28^{+0.38}_{-0.41}$	$-0.46^{+0.60}_{-0.28}$
095752.17+015120.1	BL	4.16	Z	$46.28^{+0.69}_{-0.10}$	$8.71^{+0.41}_{-0.42}$	$-0.54^{+0.53}_{-0.36}$
095752.17+015120.1	BL	4.17	I	$46.26^{+0.54}_{-0.07}$	$8.66^{+0.38}_{-0.44}$	$-0.51^{+0.52}_{-0.31}$
095753.49+024736.1	BL	3.61	I	$46.24^{+0.75}_{-0.27}$	$8.00^{+0.49}_{-0.40}$	$0.12^{+0.69}_{-0.46}$
095754.11+025508.4	BL	1.57	S	$46.21^{+0.66}_{-0.49}$	$8.70^{+0.39}_{-0.41}$	$-0.61^{+0.65}_{-0.32}$
095754.70+023832.9	BL	1.60	S	$46.14^{+0.54}_{-0.24}$	$8.72^{+0.40}_{-0.41}$	$-0.69^{+0.47}_{-0.39}$

Notes.
[a] "BL" refers to a broad-line AGN, "NL" is a narrow-line AGN, and "OD" is a lineless or optically dull AGN.
[b] "S" means the spectrum and redshift are from the SDSS archive, "I" is from the COSMOS Magellan/IMACS campaign (Trump et al. 2009a), and "Z" is from the zCOSMOS VLT/VIMOS campaign (Lilly et al. 2007).

(This table is available in its entirety in a machine-readable form in the online journal. A portion is shown here for guidance regarding its form and content.)

("Ell2") and bluest ("Sd") normal galaxy templates of Polletta et al. (2007) are additionally used as extreme hosts to estimate the possible error contribution from choosing the wrong host template (described in Section 3.3).

It is possible that a few of the narrow-line and lineless AGNs might have very blue starbursting hosts, although such galaxies are uncommon at $z < 1$. An extremely blue, UV-emitting host would cause us to overestimate the accretion disk emission and consequently overestimate the accretion rate. Since the narrow-line and lineless AGNs have lower accretion rates than broad-line AGNs (as we discuss in Section 4), it would only strengthen our conclusions if their true accretion rates were even lower. It is also possible that very red, dusty hosts could cause us to underestimate the true accretion rates for narrow-line and lineless AGNs. However, a dusty host should cause the AGN to appear extincted, and our sample of AGNs generally has low measured absorption (see Section 2.1). In addition, restricting our fitting to $1\,\rm eV < E < 100\,eV$ ($12{,}400\,\text{Å} > \lambda > 124\,\text{Å}$) already means that a normal elliptical galaxy (like our "Ell2" template) contributes very little flux where we fit the accretion disk.

While broad-line AGNs are likely to have some host contribution, we cannot use surface brightness fitting to estimate their host luminosity because they are at high redshift and their point source overwhelms their extended emission (Gabor et al. 2009). However, at the peak of the accretion disk emission for a broad-line AGN ($\sim$ 3000 Å or 4 eV), the host galaxy contributes <20% of the emission (e.g., Bentz et al. 2006). Because we additionally restrict our accretion disk fitting to $1\,\rm eV < E < 100\,eV$ ($12{,}400\,\text{Å} > \lambda > 124\,\text{Å}$), we can assume that the error from not subtracting the host for broad-line AGNs is typically <0.1 dex.

We shift the observed (and host-subtracted, for narrow-line and lineless AGNs) photometry to the rest frame from the measured spectroscopic redshift, and convert the magnitudes or fluxes to luminosities. We then fit an accretion disk model to the optical/UV emission within the range $1\,\rm eV < E < 100\,eV$ ($2.4 \times 10^{14}\,\rm Hz < \nu < 2.4 \times 10^{16}$ Hz, or $12{,}400\,\text{Å} > \lambda > 124\,\text{Å}$) and a power law representing the X-ray corona emission to the rest-frame X-ray data. We measure the total bolometric luminosity from the sum of the disk luminosity (given by the analytic solution in Equation (3) below) and the power-law luminosity from $4E_{\rm peak} < E < 250$ keV (where $E_{\rm peak}$ is the peak energy of the best-fit disk model). While the X-ray background requires a high-energy cutoff for AGNs in the few hundreds of keV (Gilli et al. 2007), measurements of the cutoff energy exist for only $\sim$15 AGNs and vary from 50 to 500 keV (Perola et al. 2002; Molina et al. 2006). We choose 250 keV as an intermediate value, although any cutoff from 50 to 500 keV does not greatly influence our results. Our AGNs have typically flat X-ray spectra with $\Gamma_X \sim 2$, and so changing the X-ray cutoff energy by a factor of 0.2–2 effectively changes the integrated X-ray luminosity by the same factor of a few. Because the X-ray and disk luminosities are roughly comparable (see Figure 2), this results in less than a factor of two change in the total accretion luminosity—much less than the $\sim$0.5 dex errors we compute for our estimated $L_{\rm int}/L_{\rm Edd}$ (see Section 3.3).

We use the accretion disk model of Gierliński et al. (1999), which improves upon a basic blackbody accretion disk by including a correction for relativistic effects. (The Gierliński et al. 1999 model is the "diskpn" model of the Xspec X-ray fitting software.) This model is based on the pseudo-Newtonian gravitational potential $\Phi = -GM/(R-2R_g)$ (Pacyński & Wiita 1980), where $R_g = GM/c^2$. From Gierliński et al. (1999), the model takes the form:

$$L = K E^4 \int_{r_{\rm in}}^{\infty} \frac{r\,dr}{\exp[E/kT(r)] - 1} \qquad (1)$$

where $r = R/R_g$ and we assume the innermost stable orbit $r_{\rm in} = 6$. The temperature depends on radius as

$$T(r) = \frac{T_0}{c_0}\left[\frac{r-2/3}{r(r-2)^3}\left(1 - \frac{3^{3/2}(r-2)}{2^{1/2}r^{3/2}}\right)\right]^{1/4}, \qquad (2)$$

with $c_0 \simeq 0.1067$ and $T_0 \propto M_{\rm BH}\dot{m}^{1/4}$. The coefficient K depends on inclination angle, coronal absorption, and the color-to-effective-temperature ratio. Rather than estimate these values, we assume that K is a constant, computed by simply scaling the

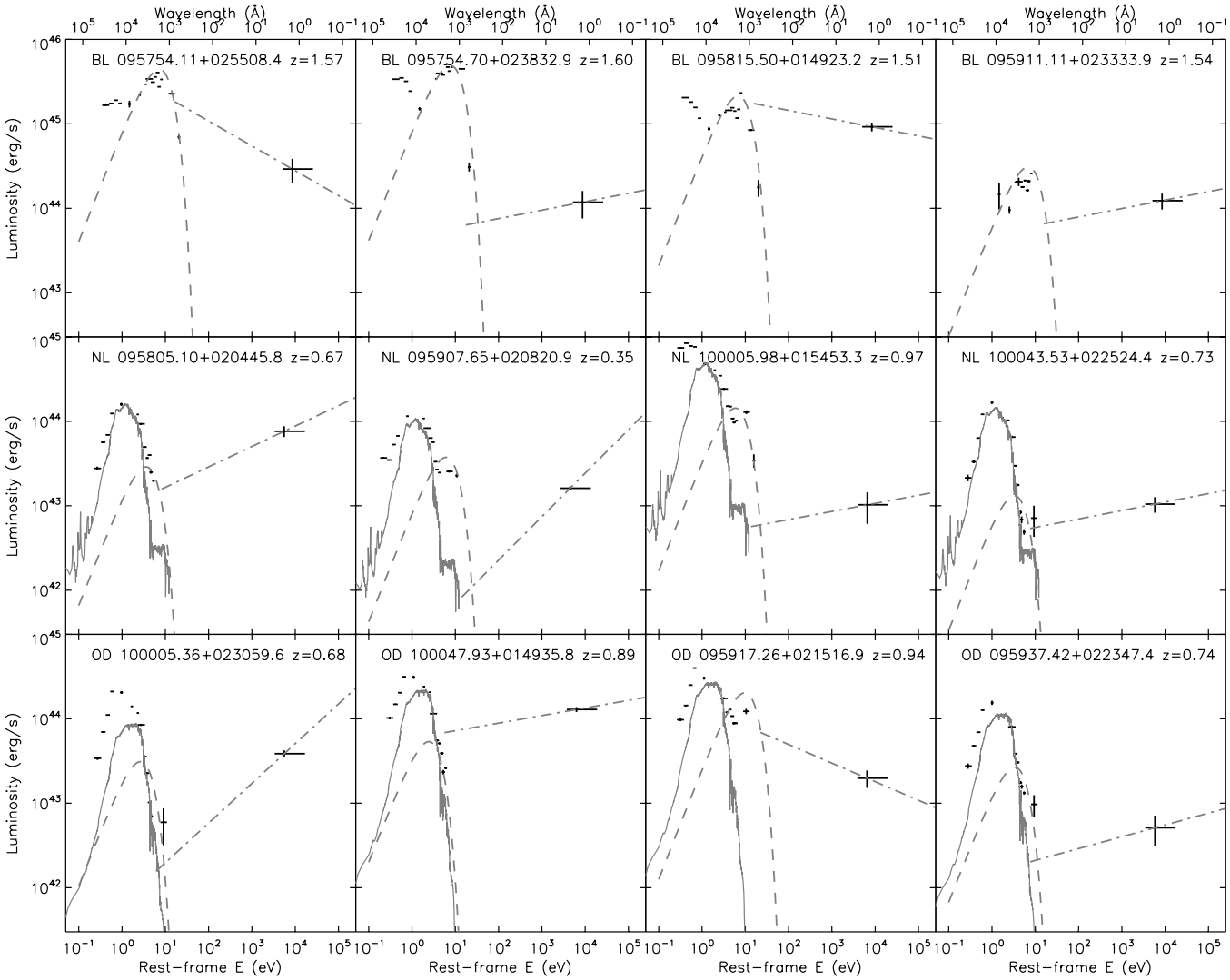

Figure 2. Multiwavelength photometry and model fits for 12 example AGNs. The top four panels are broad-line AGNs (represented by "BL"), the middle four are narrow-line AGNs (represented by "NL"), and the bottom four are lineless "optically dull" AGNs (represented by "OD"). In each panel, the dashed line is the best-fit accretion disk model and the dot-dashed line is the X-ray power-law fit. The X-ray power-law slope comes from the X-ray spectral fit, although we show only the X-ray photometry data in this figure. Estimated host SEDs are shown by solid lines for the narrow-line and lineless AGNs. We fit only at $E > 1$ keV in order to ignore the reprocessed IR emission, and so the longest-wavelength photometry data (especially the IRAC channels) are not fit by our models.

model to our data. T_0 is the sole free parameter. In our analyses below we refer to $E_{\rm peak}$, the peak energy of the disk, rather than T_0, and, in general, $kT_0 \simeq E_{\rm peak}/24$. We find the best-fit disk model in terms of T_0 by minimizing the χ^2 function. While most of the best-fit disk models have significant emission at $E < 1$ eV, we restrict the fit to 1 eV $< E <$ 100 eV to mitigate the effects of a contaminating torus and/or host galaxy light.

Note that the relation $T_0 \propto M_{\rm BH}\dot{m}^{1/4}$ above means that the disk temperature is constrained not only by the photometry but also by the black hole mass. In practice this prevents our fits from resulting in unphysically hot accretion disks, since disks peaking at energies much higher than ∼4 eV (3000 Å) would require unphysically small black hole masses. This is especially important to note because about one-third of the sample lacks *GALEX* UV detections, and, as a result, the declining high-energy slope is not well constrained by the photometry for low-redshift AGNs. The black hole mass error (∼ 0.4 dex) is used during the bootstrapped uncertainty measurements for the accretion disk temperature and luminosity.

The total disk luminosity is calculated analytically (see Appendix A of Gierliński et al. 1999):

$$L_{\rm disk} = K\frac{h^3c^2}{16\pi}\left(\frac{T(r_{\rm in})}{c_0}\right)^4. \quad (3)$$

Errors in both $E_{\rm peak}$ and $L_{\rm disk}$ are found by bootstrapping 1000 fits to the resampled data.

To characterize the X-ray corona emission, we use the X-ray spectral fits described in Section 2.1. Each X-ray spectrum is fit as an intrinsically absorbed power law with Galactic absorption ($N_{\rm H,gal} = 2.6 \times 10^{20}$ cm^2 in the direction of the COSMOS field). We use the photon index Γ_X to represent the power-law slope, such that $L_\nu = L_0\nu^{1-\Gamma}$. Figure 1 shows that the typical $\Gamma_X \simeq 1.9 \pm 0.4$, and we assume this slope for AGNs with too few X-ray counts for a good fit. We calculate the total X-ray luminosity by integrating the power-law model over $4E_{\rm peak} < E < 250$ keV (where $E_{\rm peak}$ is the energy peak of the disk model) using the analytic solution:

$$L_X = L_0/(2-\Gamma) \times [(250\,{\rm keV}/h)^{2-\Gamma} - (4E_{\rm peak}/h)^{2-\Gamma}]. \quad (4)$$

The total bolometric luminosity is simply the sum of the integrated accretion disk and X-ray power-law components $L_{\rm int} = L_{\rm disk} + L_X$.

Figure 2 shows a representative sample of broad-line, narrow-line, and lineless SEDs with model fits. Note that emission lines and variability (the various photometric data were taken over three years) mean that our simple accretion disk model is not a perfect fit: some of the optical/UV data differ from the model fit by up to 0.2 dex. However, such small errors in individual photometry points are negligible compared to the >0.4 dex total errors we estimate for $L_{\rm int}$ (see Figure 4 and Section 3.3). In general, the accretion disk plus X-ray power-law model provides an accurate, physically motivated fit to the data.

3.2. Black Hole Mass Estimates

For Type 1 AGNs, we estimate black hole masses using the scaling relations of Vestergaard & Osmer (2009) for the Mg II broad emission line and Vestergaard & Peterson (2006) for the Hβ and C IV broad emission lines. These relations estimate black hole mass from single-epoch spectra by employing the correlation between the radius of the BLR and the continuum luminosity, $R_{\rm BLR} \sim L^{0.5}$, observed in local AGNs with reverberation mapping (Bentz et al. 2006; Kaspi et al. 2007). In general, masses estimated from the scaling relations are accurate to ~0.4 dex (Vestergaard & Peterson 2006; Shen et al. 2008) and agree with local AGN masses from dynamical estimators (Davies et al. 2006; Onken et al. 2007) and the $M_{\rm BH}$–$\sigma*$ correlation (Onken et al. 2004; Greene & Ho 2006). The scaling relations take the form of Equation (5), with λL_λ in units of 10^{44} erg s^{-1} and $v_{\rm FWHM}$ in units of 1000 km s^{-1}; $A = 6.91$, $B = 0.50$, and $\lambda = 5100$ Å for Hβ; $A = 6.86$, $B = 0.50$, and $\lambda = 3000$ Å for Mg II; $A = 6.66$, $B = 0.53$, and $\lambda = 1350$ Å for C IV:

$$\log\left(\frac{M_{\rm BH}}{M_\odot}\right) = A + B\log(\lambda L_\lambda) + 2\log(v_{\rm FWHM}). \quad (5)$$

Black hole masses for the Type 1 AGNs with Magellan/IMACS or SDSS spectra in COSMOS have already been published (Trump et al. 2009b), and we repeat the same techniques for Type 1 AGNs with VLT/VIMOS spectra. Briefly, a power-law fit plus iron emission is fit to each AGN. The continuum luminosity is estimated directly from the continuum fit, while the velocity widths are computed from Gaussian fits to the continuum-subtracted emission lines. Some objects also have black hole masses from Merloni et al. (2010); for these objects, our masses are consistent with a random scatter of only ~0.4 dex: equivalent to the intrinsic scatter of the scaling relations (see Figure 3 of Trump et al. 2009b). Marconi et al. (2008) showed that the scatter in $M_{\rm BH}$ from the scaling relations might decrease to 0.2 dex if radiation pressure is taken into account. Replacing the scaling relations from Equation (5) with those of Marconi et al. (2008) would tighten the distribution of $L_{\rm int}/L_{\rm Edd}$ estimates for broad-line AGNs about $L_{\rm int}/L_{\rm Edd} \sim 0.3$. This has no impact on the $M_{\rm BH}$ estimates for narrow-line and lineless AGNs and does not affect the difference in $L_{\rm int}/L_{\rm Edd}$ between the broad-line sample and the narrow-line and lineless AGN sample.

Estimating black hole masses for AGNs without broad emission lines requires secondary estimators. We employ the relationship between $M_{\rm BH}$ and rest-frame K-band host bulge luminosity (Graham 2007):

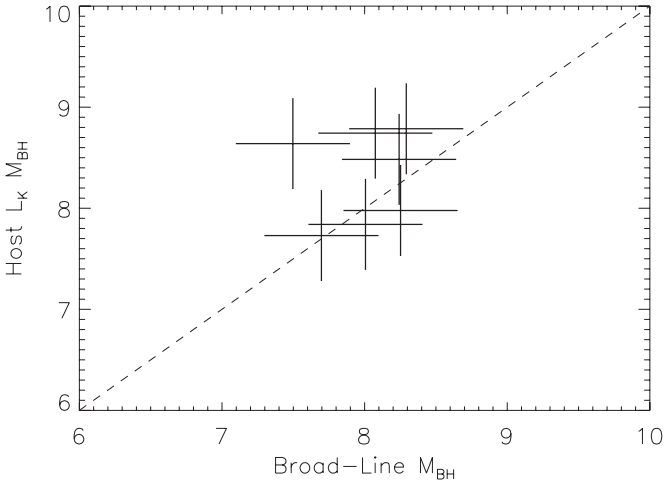

Figure 3. Black hole mass estimates from both the host L_K and the broad-line scaling relations for the seven broad-line AGNs with detected host galaxies from Gabor et al. (2009). For all but one AGN, both $M_{\rm BH}$ estimates agree within $\lesssim 1\sigma$ (for the remaining object, the two estimates differ by only $\sim 2\sigma$). From these AGNs, and the sets of nearby AGNs with similarly consistent masses from both estimators (Onken et al. 2004; Greene & Ho 2006), it is unlikely that the different mass estimators cause bias between broad-line and narrow-line/lineless AGNs.

$$\log\left(\frac{M_{\rm BH}}{M_\odot}\right) = 0.93(\log(L_K) - 0.3z) - 32.30, \quad (6)$$

with L_K in units of erg s^{-1}. The $M_{\rm BH}$–$L_{K,\rm bulge}$ relation comes from the more fundamental $M_{\rm BH}$–M_* relation, since rest-frame K bulge luminosity is correlated with M_* (e.g., Ilbert et al. 2010). We add an additional $-0.3z$ term to the relation (Graham 2007) in order to account for the evolution in the M_*/L_K ratio, $\log(M_*/L_K) \propto -0.3z$ (Arnouts et al. 2007). We measure rest-frame L_K from the host galaxy template from the multiwavelength SED fit (described above in Section 3.1). The early-type template for the lineless AGNs is, by definition, bulge dominated, and so $L_{K,\rm bulge} = L_{K,\rm host}$. The S0 template used for the narrow-line AGNs, however, has a significant disk component, and so we take $L_{K,\rm bulge} = 0.5\,L_{K,\rm host}$. The intrinsic error in the $M_{\rm BH} - L_K$ is 0.35 dex (Graham 2007). We do not correct the $M_{\rm BH}$ estimates for any evolution in the $M_{\rm bulge}$–$M_{\rm BH}$ relation because measuring $M_{\rm bulge}$–$M_{\rm BH}$ evolution has proved difficult due to significant biases in most tests (Lauer et al. 2007; Shen & Kelly 2010). Besides, although some evidence for evolution to $z \sim 3$ exists (Decarli et al. 2010), there is probably little or no evolution to $z \sim 1.5$ (Jahnke et al. 2009) and our narrow-line and lineless AGNs lie at $z < 1$.

Because we use different mass estimators for broad-line and narrow-line/lineless AGNs, it is important to demonstrate that the two methods agree. Seven of our broad-line AGNs have detected host galaxies from the decompositions of Gabor et al. (2009), and for these AGNs we compare $M_{\rm BH}$ estimates from the broad-line scaling relations and from the host galaxy rest-frame L_K in Figure 3. The $M_{\rm BH}$ estimates from broad lines and L_K agree within $<2\sigma$ for all objects (indeed, estimates for all objects but one agree within $<1\sigma$). In addition to the seven broad-line AGNs in our sample, both the broad-line and host galaxy $M_{\rm BH}$ estimators have been shown to produce consistent masses for nearby AGNs (Onken et al. 2004; Greene & Ho 2006). It is particularly unlikely that either of the estimators is systematically off by a factor of 100. Therefore, we are confident that the factor of 100 difference in $L_{\rm int}/L_{\rm Edd}$ for broad-line

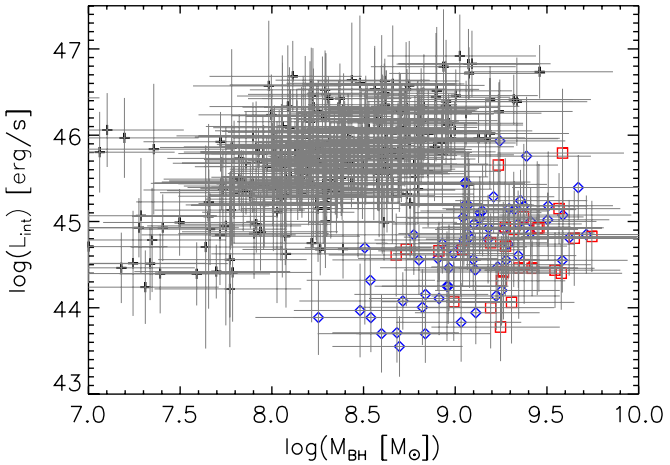

Figure 4. Intrinsic luminosity $L_{\rm int}$ with black hole mass $M_{\rm BH}$ for the AGN sample. Broad-line AGNs are shown by black crosses, narrow-line AGNs by blue diamonds, and lineless AGNs by red squares. Errors are calculated as described in Section 3.3. Narrow-line and lineless AGNs generally have higher masses, due to the COSMOS selection limits, but they also have lower luminosities as expected because of downsizing.

(A color version of this figure is available in the online journal.)

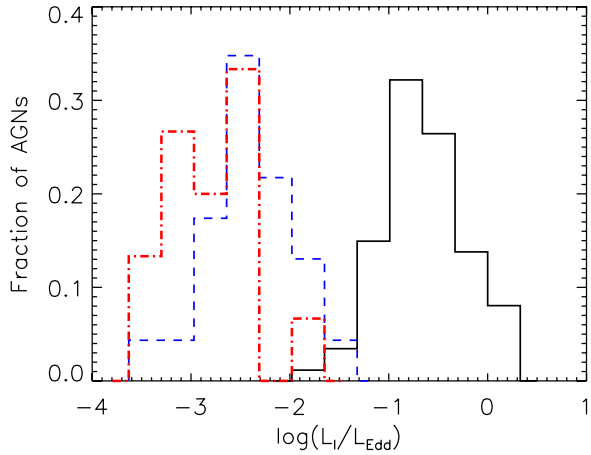

Figure 5. Distribution of calculated specific accretion rates ($L_{\rm int}/L_{\rm Edd}$) for the 82 unobscured ($N_{\rm H} < 10^{22}$ cm^{-2}) broad-line AGNs (black histogram), 24 narrow-line AGNs (blue dashed histogram), and 12 lineless AGNs (red dotted histogram). Narrow-line and lineless AGNs have significantly lower accretion rates than broad-line AGNs. The $L_{\rm int}/L_{\rm Edd} \gtrsim 0.01$ limit for broad-line AGNs is not a selection effect (Trump et al. 2009b).

(A color version of this figure is available in the online journal.)

and narrow-line/lineless AGNs in Section 4 (see, for example, Figure 5) is a physical effect, robust beyond the choice of black hole mass estimator.

We highlight the range and limitations of the AGN sample in Figure 4, which shows bolometric luminosities and black hole masses for the broad-line, narrow-line, and lineless AGNs. Objects in the upper left have the highest specific accretion rates, while those in the lower right are weakly accreting AGNs. While the total sample spans three orders of magnitude in both luminosity and black hole mass, our narrow-line and lineless AGNs are generally less luminous and more massive than broad-line AGNs. The lack of low-mass narrow-line and lineless AGNs is due to the selection limits of the survey; such objects are too faint to be detected in COSMOS. It is suggestive that these higher mass narrow-line and lineless AGNs are at $z < 1$ and are less luminous, which is consistent with "downsizing," i.e., more massive AGNs become less active at lower redshifts (Ueda et al. 2003; Brandt & Hasinger 2005; Bongiorno et al. 2007).

Figure 4 shows that, at a given mass or luminosity, there are generally all types of AGNs present in our sample. For this reason we do not expect that the differences between broad-line and narrow-line/lineless AGNs are biased by selected samples from different masses or luminosities. In addition, despite the different redshifts of most broad-line and narrow-line/lineless AGNs, we do not expect their differences to be caused by redshift. There is evidence that AGN obscuration properties depend on redshift (Treister et al. 2009; Trump et al. 2009a), but these AGNs are unobscured. The AGN central engine, meanwhile, does not change with redshift in terms of ionization parameters (Dietrich & Hamann 2004; Vestergaard 2004), SEDs (Vignali et al. 2003; Richards et al. 2006; Kelly et al. 2008), or metallicity (Simon & Hamann 2010). Limiting the sample to $z < 1$, $8.5 < \log(M_{\rm BH}) < 9$, or $44 < \log(L_{\rm int}) < 45$ does not significantly change the differences between the broad-line and narrow-line/lineless AGN samples seen in Figures 5, 6, 7, or 8.

3.3. Error Budget

We estimate errors for each of our specific accretion rates, propagating the errors from both the intrinsic luminosity estimate and the black hole mass estimate. Our intrinsic luminosity is subject to three major uncertainties.

1. *Photometry errors,* $\sigma_{\rm phot}$. We measure the error contribution of the photometry by bootstrapping, fitting our model SED to 1000 realizations of randomly drawn photometry values distributed according to the measurement errors. In general, $\sigma_{\rm phot} \sim 0.1$ dex.
2. *Errors in the host subtraction,* $\sigma_{\rm host}$. For broad-line AGNs, we do not subtract a host component and assume that any remaining galaxy light overestimates the intrinsic luminosity (from the UV and X-ray) by only <0.1 dex (see Section 3.1). For narrow-line and lineless AGNs, we estimate $\sigma_{\rm host}$ from the difference in the resultant $L_{\rm int}$ when using a very red ("Ell2") and a very blue ("Sd") template from Polletta et al. (2007). Since the accretion disk is fit only at $E > 1$ eV, where there is little host emission (even from the "Sd" galaxy), this error is usually insignificant ($\sigma_{\rm host} \lesssim 0.1$ dex).
3. *Incorrect* $L_{\rm int}$ *resulting from extinction,* $\sigma_{\rm ext}$. Underestimated extinction will make the true $L_{\rm disk}$ greater than our estimate because optical/UV light will be missed, but will make the true L_X lower than our estimate because the power-law slope will be too hard. Because we restrict our main analyses to unobscured ($N_{\rm H} < 10^{22}$ cm^{-2}) AGNs, we assume that this error is <0.1 dex (see Section 2.1).

The black hole estimate is subject to two major uncertainties.

1. *Intrinsic errors in the* $M_{\rm BH}$ *relations,* $\sigma_{\rm rel}$. For broad-line AGNs, the intrinsic error in the scaling relations is 0.4 dex (Vestergaard & Peterson 2006), such that $\sigma_{\rm rel} = 2.5 M_{\rm BH}$. For narrow-line and lineless AGNs, we use the $M_{\rm BH}$–$L_{K,\rm host}$ relation, and its associated intrinsic scatter is 0.35 dex (Graham 2007), such that $\sigma_{\rm rel}/M_{\rm BH} = 2.2$. These errors dominate the error in $L_{\rm int}/L_{\rm Edd}$, except for highly absorbed AGNs with $N_{\rm H} > 10^{22.5}$ cm^{-2}.
2. *Measurement error in the luminosity used in the scaling relation,* $\sigma_{\rm lum}$. For broad-line AGNs, this is the measured continuum luminosity associated with the appropriate scaling relation, estimated by Trump et al. (2009b) as $\sigma_{\rm lum} \sim 0.05$ dex. Since $M_{\rm BH} \propto L^{0.5}$, $\sigma_{\rm lum} = 1.3 M_{\rm BH}$ for broad-line

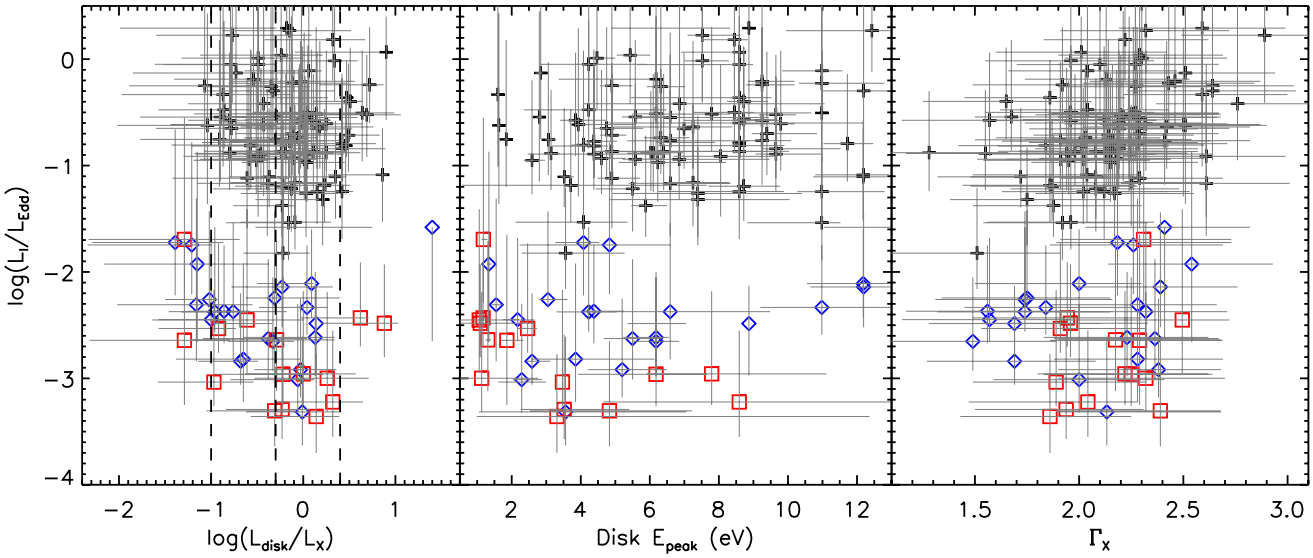

Figure 6. Specific accretion rate $L_{\rm int}/L_{\rm Edd}$ and the ratio of disk-to-corona emission $\log(L_{\rm disk}/L_X)$, disk temperature $E_{\rm peak}$, and X-ray photon index Γ_X for the 118 unobscured AGNs with $N_{\rm H} < 10^{22}$ cm^{-2}. In each panel, black crosses represent broad-line AGNs, blue diamonds are narrow-line AGNs, and red squares are lineless AGNs. The dashed lines in the left panel show lines of $\alpha_{\rm OX} = 1.0, 1.5, 2.0$, assuming $E_{\rm peak} = 6$ keV and $\Gamma_X = 1.9$. Unobscured narrow-line and lineless AGNs have ∼100 times lower accretion rates than broad-line AGNs, as well as significantly cooler and somewhat weaker accretion disks.

(A color version of this figure is available in the online journal.)

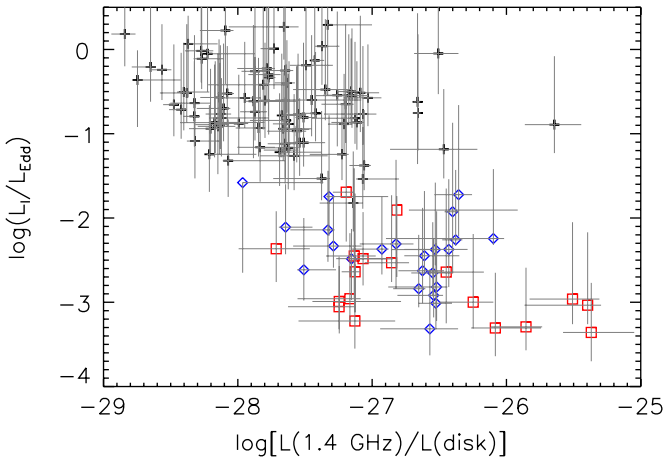

Figure 7. Accretion rate with a measure of radio brightness: the ratio of radio luminosity to disk luminosity for the 118 unobscured ($N_{\rm H} < 10^{22}$ cm^{-2}) AGNs in our sample. Broad-line AGNs are shown by black crosses, narrow-line AGNs by blue diamonds, and lineless AGNs by red squares. Narrow-line and lineless AGNs, at lower accretion rates than broad-line AGNs, tend to be more radio luminous compared to their accretion disk luminosity.

(A color version of this figure is available in the online journal.)

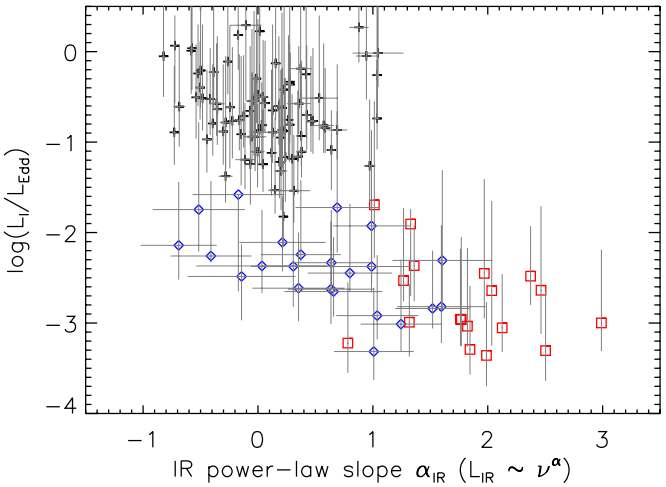

Figure 8. Accretion rate with the power-law slope of the $1 < \lambda < 10\,\mu$m IR emission for the 118 unobscured ($N_{\rm H} < 10^{22}$ cm^{-2}) AGNs. As in previous figures, black crosses are broad-line AGNs, blue diamonds are narrow-line AGNs, and red squares are lineless AGNs. We measure the slope $\alpha_{\rm IR}$ as $L \sim \nu^{\alpha}$, corresponding to the slope β used in the power-law selection of Donley et al. (2007) as $\beta = \alpha_{\rm IR} - 1$. Most high accretion rate ($L_{\rm int}/L_{\rm Edd} > 0.01$) AGNs have IR power-law slopes corresponding to a dusty torus ($\alpha_{\rm IR} < 0.5$). Of $L_{\rm int}/L_{\rm Edd} < 0.01$ AGNs, however, half the narrow-line and all of the lineless AGNs lack the torus signature.

(A color version of this figure is available in the online journal.)

AGNs. For other AGNs the $\sigma_{\rm lum}$ comes from our measured $L_{K,\rm rest}$. We estimate this error for the narrow-line and lineless AGNs from 1000 fits to the randomly subsampled data and find that the error is generally insignificant compared to the intrinsic error ($\sigma_{\rm lum} \sim 0.05$ dex). Note that the contribution from error in $v_{\rm FWHM}$ to $M_{\rm BH}$ in broad-line AGNs is also negligible, since for our AGNs $\sigma(v_{\rm FWHM}) < 0.2 v_{\rm FWHM}$ (Trump et al. 2009b).

The total error in specific accretion rate, σ_λ, is then given by

$$\frac{\sigma_\lambda^2}{\lambda^2} = \frac{\sigma_{\rm phot}^2 + \sigma_{\rm host}^2}{L_{\rm int}^2} + \frac{\sigma_{\rm rel}^2 + \sigma_{\rm lum}^2}{M_{\rm BH}^2}. \quad (7)$$

We measure the total error by bootstrapping, with 1000 fits to the resampled data. In each fit, we allow all of the above parameters to vary according to their error. The intrinsic error in the $M_{\rm BH}$ relations ($\sigma_{\rm rel}$) dominates the error. The average errors are ∼0.5 dex, compared to the ∼4 dex range in $L_{\rm int}/L_{\rm Edd}$ for the AGNs in the sample.

4. THE PHYSICAL EFFECTS OF SPECIFIC ACCRETION RATE

The distribution of $L_{\rm int}/L_{\rm Edd}$ for the 118 unobscured AGNs is shown in Figure 5. It is immediately evident that unobscured narrow-line and lineless AGNs accrete much more weakly than

broad-line AGNs, with specific accretion rates differing, on average, by ∼2 orders of magnitude. This suggests that many narrow-line and lineless AGNs are not simply geometrically obscured versions of broad-line AGNs but instead have fundamentally different accretion physics, which we examine in more detail below.

The large ∼0.5 dex errors in accretion rate artificially broaden the distributions, such that the intrinsic distributions are likely narrower than the histograms in Figure 5 appear (although many $L_{\rm int}/L_{\rm Edd} \lesssim 10^{-3}$ narrow-line and lineless AGNs could be too faint for the COSMOS X-ray and spectroscopy limits). The $L_{\rm int}/L_{\rm Edd} \gtrsim 0.01$ limit for broad-line AGNs could be partially explained by selection effects (Kelly et al. 2010), since low accretion rate AGNs are typically less luminous. However, at the highest masses ($M_{\rm BH} \sim 10^9\,M_\odot$), broad-line AGNs with $L_{\rm int}/L_{\rm Edd} \lesssim 0.01$ must be very rare (Kollmeier et al. 2006; Trump et al. 2009b). Meanwhile, unobscured narrow-line and lineless AGNs are generally limited by $L_{\rm int}/L_{\rm Edd} \lesssim 0.01$. With low X-ray column densities and low accretion rates, these objects have similar properties to the "naked" Type 2 AGNs of Tran (2003), which additionally lack reflected broad emission lines in spectropolarimetry (see also Gliozzi et al. 2007; Wang & Zhang 2007). We expect that the X-ray-unobscured low accretion rate AGNs would similarly lack reflected broad emission lines. Our method cannot accurately estimate $L_{\rm int}/L_{\rm Edd}$ for obscured AGNs, but, following a unified model with geometric obscuration (e.g., Antonucci 1993), obscured narrow-line AGNs would likely have accretion rates comparable to our broad-line AGNs.

We can compare the specific accretion rates and AGN types with the physical parameters of our model fits, namely, the ratio of disk-to-power-law emission, the peak energy of the accretion disk model, and the X-ray power-law slope. These quantities are particularly useful in unifying AGNs in terms of their accretion physics. Figure 6 shows the specific accretion rate with these parameters for each AGN type. The values of $L_{\rm disk}/L_X$ can be roughly translated to values of $\alpha_{\rm OX}$, with $\alpha_{\rm OX} = -0.384\log[L_\nu(2500\,\text{Å})/L_\nu(2\,\text{keV})]$ (Tananbaum et al. 1979; Kelly et al. 2008). The left panel of Figure 6 shows tracks of $\alpha_{\rm OX} = 1.0, 1.5, 2.0$, assuming $E_{\rm peak} = 6$ keV and $\Gamma_X = 1.9$ (hotter disks and softer X-ray slopes increase $\alpha_{\rm OX}$). Once again, narrow-line and lineless AGNs have lower specific accretion rates, and they also tend to have lower $L_{\rm disk}/L_X$ and $E_{\rm peak}$.

We can determine the significance of any differences in $L_{\rm disk}/L_X$, $E_{\rm peak}$, and Γ_X between rapidly accreting broad-line AGNs and weakly accreting narrow-line and lineless AGNs by comparing their mean values and considering the scatter of each sample. Given mean values μ_1 and μ_2 and associated scatters σ_1 and σ_2 for each set, the significance of their difference is given by $(\mu_1 - \mu_2)/\sqrt{(\sigma_1^2/N_1 + \sigma_2^2/N_2)}$, where N_1 and N_2 are the numbers of AGNs in each sample. The broad-line AGNs have $\mu(\log(L_{\rm disk}/L_X)) = -0.14 \pm 0.44$ while the narrow-line and lineless AGNs have $\mu(\log(L_{\rm disk}/L_X)) = -0.38 \pm 0.64$, so that their difference is marginally significant at 2.1σ. The difference in $E_{\rm peak}$ is more significant: the broad-line AGNs have $\mu(\log(E_{\rm peak})) = 0.80 \pm 0.20$ and the narrow-line/lineless AGNs have $\mu(\log(E_{\rm peak})) = 0.59 \pm 0.37$, so that the difference is significant to 3.3σ. From this we can conclude that a transition from weakly accreting narrow-line and lineless AGNs to the rapidly accreting broad-line AGNs results in significantly hotter and marginally brighter emission from the accretion disk.

There is no significant difference between X-ray slope Γ_X for the different AGN types: mean $\Gamma_X = 2.14 \pm 0.29$ for rapidly accreting broad-line AGNs and mean $\Gamma_X = 2.05 \pm 0.29$ for weakly accreting narrow-line and lineless AGNs (the difference is only 1.2σ significant). This is in contrast to the prediction of Hopkins et al. (2009), who suggest that harder X-ray slopes are expected for radiatively inefficient accretion flows (RIAFs) expected at low accretion rates. The appearance of an RIAF at inner radii might produce more X-ray emission, as we discuss in Section 4.1 below, but this emission probably has a similar power-law slope to the X-ray corona present in broad-line AGNs with high accretion rates. This is unsurprising, since both the RIAF and the corona are thought to be ionized plasmas with X-ray emission from inverse Compton scattering and/or bremsstrahlung. We can conclude that the onset of an RIAF in unobscured narrow-line and lineless AGNs with accretion rates of $10^{-4} < L_{\rm int}/L_{\rm Edd} < 10^{-2}$ do not cause harder X-ray power-law slopes.

4.1. Physics of the Accretion Disk

As accretion rate increases from lineless and narrow-line to broad-line AGNs, the disk temperature significantly increases and its brightness with respect to the X-rays marginally increases. An increase in temperature with accretion rate is expected for a thin accretion disk, which has $T_{\rm max} \propto \dot{m}^{1/4}$ (Shakura & Sunyaev 1973). We discuss below how the onset of an RIAF could also cause apparent cooler disk emission. Both an increase in temperature and in $L_{\rm disk}/L_X$ with accretion rates would contribute to the observed increase of $\alpha_{\rm OX}$ (the ratio of rest-frame UV to X-ray emission) with accretion rate (Kelly et al. 2008; Young et al. 2010). In our previous work (Trump et al. 2009c), we suggested that the increase of $\alpha_{\rm OX}$ with accretion rate was due only to the disk luminosity decreasing with respect to the corona luminosity. While this is partly correct, the correlation is also caused by increasing disk temperatures at higher accretion rates.

AGNs with $L_{\rm int}/L_{\rm Edd} \lesssim 0.01$ are predicted to have RIAFs near the central black hole (Begelman et al. 1984; Narayan et al. 1995; Yuan 2007; Narayan & McClintock 2008). At such accretion rates, we can define a truncation radius R_t where the collisional cooling time is comparable to the accretion time. Beyond R_t, accretion will remain in a standard geometrically thin and optically thick disk with a thermal blackbody spectrum (e.g., Shakura & Sunyaev 1973). However, within R_t, there are too few collisions to couple the ions and electrons, and the gas becomes a two-temperature plasma. The electrons are cooled by bremsstrahlung, synchrotron, and Compton upscattering, while the ions remain at the virial temperature. This means the flow is geometrically thick and optically thin. The introduction of a truncation radius changes the $R_{\rm in} = 6\,R_g$ assumption for the accretion disk model, since by definition $R_{\rm in} \geqslant R_t$. The peak energy of the best-fit accretion disk model is not very sensitive to the choice of $R_{\rm in}$, although larger inner radii change the shape of the model with additional red emission. At accretion rates of $L_{\rm int}/L_{\rm Edd} \gtrsim 10^{-3}$, as in our sample, $R_t \sim 80\,R_g$ (Yuan & Narayan 2004). Using $r_{\rm in} = 80$ in the accretion disk model fitting in Section 3.1 does not change the best-fit values of $E_{\rm peak}$, although it does result in slightly better fits.

The marginal (2.1σ significant) increase of $L_{\rm disk}/L_X$ with $L_{\rm int}/L_{\rm Edd}$ might also be caused by the onset of the RIAF. As R_t expands outward, the disk emission decreases and the RIAF emission increases. The RIAF hot plasma emission is mostly X-ray bremsstrahlung and Compton upscattering (like the corona), with an additional IR synchrotron component (which we discuss in Sections 4.3). As accretion rate drops and R_t

increases, the rise of the RIAF X-ray emission compared to the optical/UV disk emission is seen as a decrease of $L_{\rm disk}/L_X$. Indeed, local low-luminosity AGNs have even lower accretion rates and larger R_t, with consequently lower $L_{\rm disk}/L_X$ ratios and cooler optical thin-disk emission (Ho 2008).

The transition to an inner RIAF also causes the disappearance of broad emission lines at $L_{\rm int}/L_{\rm Edd} \lesssim 0.01$. Nicastro (2000) was the first to elegantly show that the broad emission lines are only present above a critical accretion rate. However, Nicastro (2000) assumed that the innermost possible orbit was given by the Shakura & Sunyaev (1973) thin-disk model, $r_{\rm crit} \simeq 8.16\,R_g$. Here we follow their basic derivation, with the key difference that we use the RIAF transition radius as the innermost orbit for the presence of a BLR.

There is evidence that the BLR is part of a disk wind (e.g., Emmering et al. 1992; Murray & Chiang 1998; Elvis 2000; Elitzur & Shlosman 2006). The positions of individual broad emission lines are stratified and set by the ionizing luminosity of the continuum (e.g., Peterson & Bentz 2006; Denney et al. 2009). The base of the wind itself, however, is set by the radius at which the radiation pressure equals the gas pressure, defined by Shakura & Sunyaev (1973) as

$$\frac{r_{\rm wind}}{\left(1-r_{\rm wind}^{-0.5}\right)^{16/21}} \simeq 15.2(\alpha M)^{2/21}\left(\frac{\dot{m}}{\eta}\right)^{16/21}, \quad (8)$$

with $r_{\rm wind}$ in units of $R/(6\,R_g) = R/(6GM/c^2)$, M in units of $M_{\rm BH}/M_\odot$, α the viscosity parameter, and η the accretion efficiency. While RIAFs are expected to have strong outflows (see Section 4.2), the RIAF region is a high-temperature ionized plasma, and so any associated disk wind would not emit broad emission lines in the UV/optical. Thus, the RIAF truncation radius sets the innermost possible radius for the existence of a BLR. Assuming that $\dot{m} \simeq L_{\rm int}/L_{\rm Edd}$ and rearranging Equation (8) with $r_{\rm wind} > R_t$, $\alpha \simeq 0.1$, and $\eta \simeq 0.1$, this sets the minimum specific accretion rate for a BLR as

$$\dot{m} \gtrsim 0.013(R_t/80\,R_g)M_8^{-1/8}, \quad (9)$$

with $M_8 = M_{\rm BH}/(10^8\,M_\odot)$. We leave R_t as a free parameter since it is poorly constrained, although the best-fit RIAF models for $L_{\rm int}/L_{\rm Edd} \sim 10^{-3}$ to 10^{-2} AGNs suggest $R_t \sim 80\,R_g$ (Yuan & Narayan 2004). As an AGN drops below this minimum accretion rate, its broad lines disappear and only narrow lines (or no lines) are observed, as seen in the transition at $\log(L_{\rm int}/L_{\rm Edd}) \sim -2$ in Figures 5 and 6.

Elitzur & Ho (2009) also predict that the disk wind associated with the BLR will disappear below an accretion rate at which the outflowing velocity drops below the random velocity of the disk. Elitzur & Ho (2009) measure a BLR-disappearance accretion rate of $\log(L/L_{\rm Edd}) < C + \beta\log(L_{\rm bol})$ from the low-luminosity local AGNs of Ho (2009), with $\beta = -0.5$ and $C = 14.4$. In our sample (as well as those of Kollmeier et al. 2006; Trump et al. 2009b), the BLR disappears at $\log(L/L_{\rm Edd}) < 0.01$. For a typical bolometric luminosity of $L_{\rm int} \sim 10^{44.5}$ erg s^{-1} (also appropriate for the Kollmeier et al. 2006 sample), and assuming the same $\beta = -0.5$, this instead corresponds to $C = 20.3$, a remarkable difference of six orders of magnitude. It is unlikely that the bolometric corrections of Ho (2009) are incorrect by six orders of magnitude, and so we must conclude that the Elitzur & Ho (2009) model does not describe the disappearance of the BLR for high-luminosity AGNs. Instead, a disk wind model following Nicastro (2000) best describes the BLR disappearance as the radius of wind generation region moves within the inner RIAF region.

It must be noted that while disk wind models have had success in describing highly ionized emission and absorption lines in the UV (Proga et al. 2000; Proga & Kallman 2004), they have not been applied to optical emission lines. The Hα broad emission line almost certainly forms in a higher density, lower ionization region than the C IV and Mg II broad emission lines. In addition, there is evidence that the dynamics of the Hβ broad emission line are wildly variable, with reverberation mapping indicating infalling, virialized, and outflowing Hβ emission regions in three AGNs (Denney et al. 2009). While we do find that broad Hβ tends to be present only for $L_{\rm int}/L_{\rm Edd} \gtrsim 0.01$, and so fits in the wind/RIAF framework, we do not study Hα and cannot say if this line is described by the same physics. Indeed, Ho (2009) presents several AGNs with broad Hα emission and $L_{\rm int}/L_{\rm Edd} < 10^{-3}$. This suggests that broad Hα emission may have its origin outside the disk wind, although it is important to note that the accretion rates of Ho (2009) rely on bolometric corrections to monochromatic luminosities and so may suffer from significant systematic uncertainties.

4.2. Accretion Rate and Outflows

The gas in an RIAF is not gravitationally bound to the SMBH because the ions are not losing energy through radiation. As a result, AGNs with RIAFs are predicted to have strong radio outflows (Narayan et al. 1995; Meier 2001). The coupling between an RIAF and a strong radio outflow has been confirmed by observations of black hole binaries (Fender & Belloni 2004), and it is possible to translate these observations to AGN scales (e.g., Maccarone et al. 2003). In Figure 7, we show the AGNs of our sample with the ratio of radio-to-disk luminosity. Note that since the radio emission is coincident with the X-ray point source, we assume that it originates from the AGN, but we cannot strictly rule out other sources of radio emission (e.g., from star formation). The $L_{\rm int}/L_{\rm Edd} < 10^{-2}$ AGNs which are expected to have RIAFs tend to have higher ratios of radio-to-disk (optical/UV) luminosity. The mean $L_{\rm disk}/L_{\rm radio}$ for rapidly accreting broad-line AGNs is a factor of 10 lower than the mean $L_{\rm disk}/L_{\rm radio}$ for narrow-line and lineless AGNs, and, since the scatter in each sample is about $\sim$0.5 dex, this translates to a highly significant difference (14.9σ).

The large scatter in the $L_{\rm disk}/L_{\rm radio}$ ratio at both high and low accretion rates is likely because the radio power is additionally dependent on properties like black hole spin and orientation. But the highly significant increase in $L_{\rm disk}/L_{\rm radio}$ for low accretion rate AGNs suggests that $L_{\rm int}/L_{\rm Edd} < 10^{-2}$ AGNs with RIAFs generally have relatively brighter radio emission. Melendez et al. (2010) noticed a similar trend of increasing radio luminosity with decreasing accretion rate, using O IV as a proxy for intrinsic luminosity (e.g., Melendez et al. 2008; Diamond-Stanic et al. 2009). Many nearby radio galaxies are also measured to have low accretion rates and may even have their optical/UV emission dominated by synchrotron emission rather than a thermal disk (Chiaberge et al. 1999).

In general, the radiation and disk winds of AGNs are thought to cause feedback on galaxy scales by quenching star formation (e.g., Hopkins et al. 2006; Hopkins & Elvis 2010), while radio jets are thought to cause larger-scale feedback which can heat the cores of galaxy clusters (e.g., Fabian et al. 2002) and is observed as extended emission line regions (Fu & Stockton 2009). The fact that RIAFs tend to have stronger radio emission suggests that weakly accreting AGNs may remain important for large-

scale radio-mode feedback despite their optical/UV and X-ray luminosities. This suggests that heating cluster cores may not require bright quasars, but can be accomplished by faint AGNs (see also Hart et al. 2009). Allen et al. (2006) similarly found that several nearby weakly accreting AGNs had most of their Bondi accretion rates converted to radio outflows.

4.3. Accretion Rate and the IR "Torus"

A clumpy dust "torus" emits a unique power-law signature in the mid-IR from ∼1 to 10 μm (Nenkova et al. 2008). This was first noticed observationally as a distinct AGN locus in *Spitzer*/IRAC color–color space (Lacy et al. 2004; Stern et al. 2005), although Donley et al. (2007) show that power-law selection is the most effective way to select AGNs in the mid-IR. We compute the IR power-law slope in our AGNs from the host-subtracted observed IRAC photometry within the rest-frame wavelength range $1\,\mu\mathrm{m} < \lambda < 10\,\mu\mathrm{m}$, shown with accretion rate in Figure 8. Type 1 AGNs typically have $\alpha_{\rm IR} < 0.5$ ($\beta_{\rm IR} < -0.5$ in terms of the $f_\nu \sim \nu^\beta$ form used by Donley et al. 2007), matching the predictions of clumpy dust models (Nenkova et al. 2008). About 10% of Type 1 AGNs are "hot-dust-poor" and do not satisfy the $\alpha_{\rm IR}$ selection criterion;[13] about half of the narrow-line AGNs and all of the lineless AGNs lack this torus signature. Cardamone et al. (2008) similarly found that many X-ray AGNs did not have a mid-IR power law, although they did not track it with accretion rate. In our sample, the rapidly accreting broad-line AGNs have a mean $\alpha_{\rm IR} = 0.38 \pm 0.35$, while the weakly accreting narrow-line and lineless AGNs have a mean $\alpha_{\rm IR} = 1.26 \pm 0.72$, meaning that the two samples differ with high significance (10.7σ).

A unified model based solely on geometrical obscuration suggests that narrow-line and lineless AGNs are obscured by the same torus present in broad-line AGNs (e.g., Antonucci 1993). Instead the low accretion rate AGNs ($L_{\rm int}/L_{\rm Edd} < 0.01$) frequently lack the torus IR signature. In part, this may be because the torus power law is simply being overwhelmed by the accretion disk SED at $L_{\rm int}/L_{\rm Edd} < 0.01$. At low accretion rates, the temperature of the disk decreases and a disk with $E_{\rm peak} = 1$ eV will peak at 1.2 μm, emitting a power law of $\alpha \sim 2$ at $1\,\mu\mathrm{m} < \lambda < 10\,\mu\mathrm{m}$. In a typical broad-line AGN, the IR torus is roughly the same strength as the accretion disk (Richards et al. 2006, see also Figure 2). Since many $L_{\rm int}/L_{\rm Edd} < 0.01$ AGNs in Figure 8 have $\alpha \gtrsim 2$, they must be dominated by the accretion disk emission and have, at best, very little emission from the torus.

The weaker or missing torus in many $L_{\rm int}/L_{\rm Edd} < 0.01$ AGNs can be described in a similar fashion to the vanishing disk wind BLR in Section 4.1. There is good evidence that the outer edge of the BLR coincides with the inner edge of the clumpy dust (Netzer & Laor 1993; Suganuma et al. 2006). Some authors additionally suggest that the BLR and the clumpy dust "torus" are two components of the same wind driven off the accretion disk (e.g., Elitzur & Shlosman 2006). If the clumpy dust wind emerges from the disk at a similar radius to that calculated in Section 4.1, then we would expect the IR power-law signature to disappear at $L_{\rm int}/L_{\rm Edd} < 0.01$, just as the BLR disappears. However, many narrow-line AGNs with $L_{\rm int}/L_{\rm Edd} < 0.01$ still have negative IR power-law slopes, suggesting that there must be another source of mid-IR emission. Either there is a distant source of clumpy dust beyond the expanding RIAF or there is mid-IR synchrotron emission in the RIAF region at the base of the radio jet (as observed by Leipski et al. 2009).

[13] For more details on this population, see Hao et al. (2010).

5. A SIMPLE MODEL FOR UNIFYING AGNs BY SPECIFIC ACCRETION RATE

Figure 9 presents a simple schematic outlining the changes in AGNs from high ($L_{\rm int}/L_{\rm Edd} > 0.01$) to low ($L_{\rm int}/L_{\rm Edd} < 0.01$) accretion rate. At the top is a broad-line AGN with high accretion rate ($L_{\rm int}/L_{\rm Edd} \sim 0.1$). At these high accretion rates, the gas and dust falling into the black hole forms a thin accretion disk and a disk wind originates at $R_{\rm wind} \sim 250\,R_g$. The broad emission lines are emitted in stratified regions along this wind based on the radiation pressure (which ionizes and excites the wind material), with $R_{\rm BLR} \sim L^{0.5}$ and high-ionization lines (e.g., C IV) emitted from nearer radii than low-ionization lines (e.g., Mg II; Peterson & Bentz 2006). At higher radii, the disk wind forms clumpy dust (Nenkova et al. 2008). This dusty "torus" can obscure the AGN along lines of sight near the disk, causing an observer to see an obscured narrow-line AGN (Antonucci 1993).

The bottom of Figure 9 shows an AGN with low accretion rate ($L_{\rm int}/L_{\rm Edd} \sim 0.003$) characteristic of the unobscured narrow-line and lineless AGNs in our sample. The onset of a geometrically thick RIAF changes the picture dramatically. Because the disk wind radius is within the RIAF, there are no broad emission lines. Instead the dominant outflow is a radio jet, and AGNs with low accretion rates and RIAFs are typically more radio luminous than broad-line AGNs. The lack of a disk wind also means that there is not the typical clumpy dust "torus" seen in broad-line AGNs. However, we cannot rule out the presence of dust completely, as clumpy dust may come from another source besides the disk wind, and some $L_{\rm int}/L_{\rm Edd} \lesssim 0.01$ have the IR signature of hot dust.

6. PREDICTIONS AND FUTURE OBSERVATIONAL TESTS

The multiwavelength data of COSMOS provide many diagnostic capabilities, and we have argued that decreasing accretion rates lead to the onset of an RIAF at $\dot{m} < 0.01$ and, subsequently, stronger radio jets, a weaker torus, and the disappearance of broad emission lines. The onset of a RIAF also makes several predictions testable by future observations. In addition, the simple model in Section 5 can be more fully constrained by additional investigations.

If the BLR is truly disappearing at $\dot{m} < 0.01$, then we would expect spectropolarimetry to reveal reflected broad emission lines only in high accretion rate ($\dot{m} > 0.01$) narrow-line and lineless AGNs. Spectropolarimetry of nearby AGNs shows a dichotomy based on accretion rate, although most authors place the change from hidden broad lines to "true" Type 2 AGNs at $\dot{m} \sim 0.001$ (Tran 2003; Wang & Zhang 2007). Most likely, the difference results from the uncertain bolometric corrections used in these previous works, compared to the full-modeled SEDs used here.

Mid-IR broadband polarimetry could determine the cause of the negative IR power-law slopes in $\dot{m} < 0.01$ AGNs. If the clumpy dust "torus" is associated with the same wind that drives the BLR, it should disappear in these objects. The mid-IR signature might instead be synchrotron radiation in the RIAF at the base of the jet, which would appear polarized at the >3% level (e.g., Jannuzi et al. 1994). If no polarization is detected, then we must conclude that clumpy dust exists at higher radii

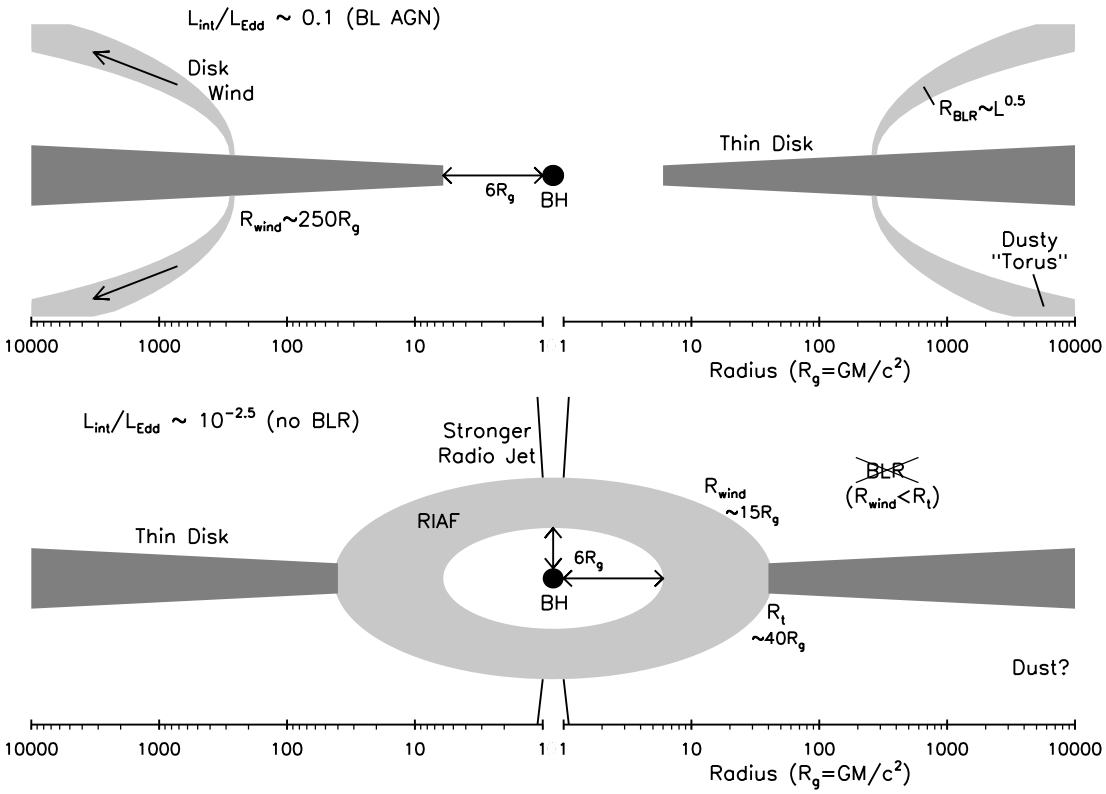

Figure 9. Schematic model showing the changes in the accretion disk from a broad-line AGN with high accretion rate ($L_{\rm int}/L_{\rm Edd} \sim 0.1$) to a narrow-line or lineless AGN with low accretion rate ($L_{\rm int}/L_{\rm Edd} \sim 0.003$). The x-axis shows the radial distance from the black hole in units of GM/c^2. The y-axis is qualitative only. At $L_{\rm int}/L_{\rm Edd} \lesssim 0.01$, the disk wind falls inside the RIAF. As a result, there are no broad emission lines, the hot dust signature becomes very different, and the radio jet becomes stronger.

than the BLR disk wind, beyond the RIAF region of $\dot{m} < 0.01$ AGNs.

It is very difficult to measure accretion rates of partially or fully obscured AGNs, and such objects are generally missed by the X-ray and optical limits of this study. However, we do make a few predictions for the accretion rates of various AGNs. If the torus is part of a disk wind that vanishes at $\dot{m} < 0.01$, then torus-obscured AGNs of the classical Antonucci (1993) unified model will have only high accretion rates ($\dot{m} > 0.01$). This is suggested by Winter et al. (2009), who showed that hard X-ray-selected Type 2 AGNs of higher accretion rates had higher $N_{\rm H}$. Obscuration by cooler dust associated with host galaxy star formation, as predicted by the observed redshift evolution in the narrow-line/broad-line AGN ratio (Treister et al. 2009; Trump et al. 2009a), could conceivably be present at any accretion rate (although it may be limited by the ability of the dusty star formation to feed the black hole; Ballantyne 2008). We might then expect that obscured AGNs with a strong mid-IR torus signature should have $\dot{m} > 0.01$, while AGNs obscured by the cooler dust associated with host galaxy star formation might have a wider range of accretion rates.

J.R.T. acknowledges support from NSF/DDEP grant 0943995, and with C.D.I. acknowledges support from NSF grant AST-0908044. B.C.K. acknowledges support from NASA through Hubble Fellowship grant HF-51243.01, awarded by the Space Telescope Science Institute, which is operated by the Association of Universities for Research in Astronomy, Inc., for NASA, under contract NAS 5-26555. Gordon Richards and Pat Hall provided useful comments on the manuscript, and we thank the anonymous referee for thorough suggestions that greatly improved the clarity of this work.

REFERENCES

Allen, S. W., Dunn, R. J. H., Fabian, A. C., Taylor, G. B., & Reynolds, C. S. 2006, MNRAS, 372, 21
Antonucci, R. 1993, ARA&A, 31, 473
Arnouts, S., et al. 2007, A&A, 476, 137
Baldwin, J. A., Phillips, M. M., & Terlevich, R. 1981, PASP, 93, 5
Ballantyne, D. R. 2008, ApJ, 685, 787
Barth, A. J., Filippenko, A. V., & Moran, E. C. 1999, ApJ, 525, 673
Begelman, M. C., Blandford, R. D., & Rees, M. J. 1984, Rev. Mod. Phys., 56, 255
Bentz, M. C., Peterson, B. M., Pogge, R. W., Vestergaard, M., & Onken, C. A. 2006, ApJ, 644, 133
Bianchi, S., Corral, A., Panessa, F., Barcons, X., Matt, G., Bassani, L., Carrera, F. J., & Jiménez-Bailón, E. 2008, MNRAS, 385, 195
Bongiorno, A., et al. 2007, A&A, 472, 443
Brandt, W. N., & Hasinger, G. 2005, ARA&A, 43, 827
Brusa, M., et al. 2010, ApJ, 716, 348
Caccianiga, A., Severgnini, P., Della Ceca, R., Maccacaro, T., Carrera, F. J., & Page, M. J. 2007, A&A, 470, 557
Cappelluti, N., et al. 2009, A&A, 497, 635
Cardamone, C. N., et al. 2008, ApJ, 680, 130
Cash, W. 1979, ApJ, 228, 939
Chiaberge, M., Capetti, A., & Celotti, A. 1999, A&A, 349, 77
Comastri, A., et al. 2002, ApJ, 571, 771
Davies, R. I., et al. 2006, ApJ, 646, 754
Decarli, R., Falomo, R., Treves, A., Labita, M., Kotilainen, J. K., & Scarpa, R. 2010, MNRAS, 402, 2453
Denney, K. D., et al. 2009, ApJ, 704, 80
Diamond-Stanic, A. M., Rieke, G. H., & Rigby, J. R. 2009, ApJ, 698, 623
Dietrich, M., & Hamann, F. 2004, ApJ, 611, 761
Di Matteo, T., Springel, V., & Hernquist, L. 2005, Nature, 433, 604

Donley, J. L., Rieke, G. H, Perez-Gonzalez, P. G., Rigby, J. R., & Alonso-Herrero, A. 2007, ApJ, 660, 167
Elitzur, M., & Ho, L. C. 2009, ApJ, 701, L91
Elitzur, M., & Shlosman, I. 2006, ApJ, 648, L101
Elvis, M. 2000, ApJ, 545, 63
Elvis, M., Schreier, E. J., Tonry, J., Davis, M., & Huchra, J. P. 1981, ApJ, 246, 20
Elvis, M., et al. 2009, ApJS, 184, 158
Emmering, R. T., Blandford, R. D., & Shlosman, I. 1992, ApJ, 385, 460
Eracleous, M., Hwang, J. A., & Flohic, H. M. 2010, ApJ, 711, 796
Fabian, A. C., Celotti, A., Blundell, K. M., Kassim, N. E., & Perley, R. A. 2002, MNRAS, 331, 369
Fender, R., & Belloni, T. 2004, ARA&A, 42, 317
Ferrarese, L., & Merritt, D. 2000, ApJ, 593, 9
Fu, H., & Stockton, A. 2009, ApJ, 690, 953
Gabor, J. M., et al. 2009, ApJ, 691, 705
Gebhardt, K., et al. 2000, ApJ, 539, 13
Gierliński, M., Zdziarski, A. A., Poutanen, J., Coppi, P. S., Ebisawa, K., & Johnson, W. N. 1999, MNRAS, 309, 496
Gilli, R., Comastri, A., & Hasinger, G. 2007, A&A, 463, 79
Gliozzi, M., Sambruna, R. M., & Foschini, L. 2007, ApJ, 662, 878
Graham, A. W. 2007, MNRAS, 379, 711
Greene, J. E., & Ho, L. C. 2006, ApJ, 641, 21
Hao, H., et al. 2010, ApJ, 724, 59
Hart, Q. N., Stocke, J. T., & Hallman, E. J. 2009, ApJ, 705, 854
Hawkins, M. R. S. 2004, A&A, 424, 519
Heckman, T. M. 1980, A&A, 87, 152
Ho, L. C. 2008, ARA&A, 46, 475
Ho, L. C. 2009, ApJ, 699, 626
Hopkins, P. F., & Elvis, M. 2010, MNRAS, 401, 7
Hopkins, P. F., Hernquist, L., Cox, T. J., di Matteo, T., Robertson, B., & Springel, V. 2006, ApJS, 163, 1
Hopkins, P. F., Hickox, R., Quataert, E., & Hernquist, L. 2009, MNRAS, 398, 333
Hornschemeier, A. F., et al. 2001, ApJ, 554, 742
Ilbert, O., et al. 2009, ApJ, 690, 1236
Ilbert, O., et al. 2010, ApJ, 709, 644
Jahnke, K., et al. 2009, ApJ, 706, 215
Jannuzi, B. T., Smith, P. S., & Elston, R. 1994, ApJ, 428, 130
Kaspi, S., Brandt, W. N., Maoz, D., Netzer, H., Schneider, D. P., & Shemmer, O. 2007, ApJ, 659, 997
Kelly, B. C., Bechtold, J., Trump, J. R., Vestergaard, M., & Siemiginowdka, A. 2008, ApJS, 176, 355
Kelly, B. C., Vestergaard, M., Fan, X., Hopkins, P. F., Hernquist, L., & Siemiginowska, A. 2010, ApJ, 719, 1315
Koekemoer, A. M., et al. 2007, ApJS, 172, 196
Kollmeier, J. A., et al. 2006, ApJ, 648, 128
Krolik, J. H., & Begelman, M. C. 1988, ApJ, 329, 702
Lacy, M., et al. 2004, ApJS, 154, 166
Lauer, T. R., Tremaine, S., Richstone, D., & Faber, S. M. 2007, ApJ, 670, 249
Leipski, C., Antonucci, R., Ogle, P., & Whysong, D. 2009, ApJ, 701, 891
Lilly, S. J., et al. 2007, ApJS, 172, 70
Maccarone, T. J., Gallo, E., & Fender, R. 2003, MNRAS, 345, L19
Magorrian, J., et al. 1998, AJ, 115, 2285
Mainieri, V., et al. 2007, ApJS, 172, 368
Maiolino, R., Marconi, A., & Oliva, E. 2001, A&A, 365, 37
Marconi, A., & Hunt, L. K. 2003, ApJ, 589, 21
Marconi, A., Risaliti, G., Gilli, R., Hunt, L. K., Maiolino, R., & Salvati, M. 2004, MNRAS, 351, 169
Marconi, A., et al. 2008, ApJ, 678, 693
Martinez-Sansigre, A., et al. 2006, MNRAS, 370, 1479
McCracken, H. J., et al. 2010, ApJ, 708, 202
Meier, D. L. 2001, ApJ, 548, L9
Melendez, M., Kraemer, S. B., & Schmitt, H. R. 2010, MNRAS, 406, 493
Melendez, M., et al. 2008, ApJ, 682, 94
Merloni, A., et al. 2010, ApJ, 708, 137
Molina, M., et al. 2006, MNRAS, 371, 821
Mor, R., Netzer, H., & Elizur, H. 2009, ApJ, 705, 298
Moran, E. C., Filippenko, A. V., & Chornock, R. 2002, ApJ, 579, L71
Murray, N., & Chiang, J. 1998, ApJ, 494, 125
Narayan, R., & McClintock, J. E. 2008, New Astron. Rev., 51, 733
Narayan, R., Yi, I., & Mahadevan, R. 1995, Nature, 374, 623
Nenkova, M., et al. 2008, ApJ, 685, 160
Netzer, H., & Laor, A. 1993, ApJ, 404, 51
Nicastro, F. 2000, ApJ, 530, L65
Onken, C. A., Ferrarese, L., Merritt, D., Peterson, B. M., Pogge, R. W., Vestergaard, M., & Wandel, A. 2004, ApJ, 615, 645
Onken, C. A., et al. 2007, ApJ, 670, 105
Pacyński, B., & Wiita, P. K. 1980, A&A, 88, 23
Pei, Y. C. 1992, ApJ, 395, 130
Perola, G. C., Matt, G., Cappi, M., Fiore, F., Guainazzi, M., Maraschi, L., Petrucci, P. O., & Piro, L. 2002, A&A, 389, 802
Peterson, B. M., & Bentz, M. C. 2006, New Astron. Rev., 50, 796
Polletta, M., et al. 2007, ApJ, 663, 81
Proga, D., & Kallman, T. R. 2004, ApJ, 616, 688
Proga, D., Stone, J. M., & Kallman, T. R. 2000, ApJ, 543, 686
Ptak, A., Terashima, Y., Ho, L. C., & Quataert, E. 2004, ApJ, 606, 173
Richards, G. T., et al. 2003, AJ, 126, 1131
Richards, G. T., et al. 2006, ApJS, 166, 470
Schinnerer, E., et al. 2007, ApJS, 172, 46
Scoville, N., et al. 2007, ApJS, 172, 38
Shakura, N. I., & Sunyaev, R. A. 1973, A&A, 24, 337
Shen, Y., Greene, J. E., Strauss, M. A., Richards, G. T., & Schneider, D. P. 2008, ApJ, 680, 169
Shen, Y., & Kelly, B. C. 2010, ApJ, 713, 41
Silverman, J. D., et al. 2009, ApJ, 696, 396
Simon, L. E., & Hamann, F. 2010, MNRAS, 407, 1826
Soltan, A. 1982, MNRAS, 200, 115
Stern, D., et al. 2005, ApJ, 631, 163
Suganuma, M., et al. 2006, ApJ, 639, 46
Tananbaum, H., et al. 1979, ApJ, 234, L9
Tran, H. D. 2001, ApJ, 554, L19
Tran, H. D. 2003, ApJ, 583, 632
Treister, E., et al. 2004, ApJ, 616, 123
Treister, E., et al. 2009, ApJ, 693, 1713
Trouille, L., Barger, A. J., Cowie, L. L., Yang, Y., & Mushotzky, R. F. 2009, ApJ, 703, 2160
Trump, J. R., et al. 2007, ApJS, 172, 383
Trump, J. R., et al. 2009a, ApJ, 696, 1195
Trump, J. R., et al. 2009b, ApJ, 700, 49
Trump, J. R., et al. 2009c, ApJ, 706, 797
Ueda, Y., Akiyama, M., Ohta, K., & Miyaji, T. 2003, ApJ, 598, 886
Vanden Berk, D. E., et al. 2001, AJ, 122, 549
Vasudevan, R. V., & Fabian, A. C. 2009, MNRAS, 392, 1124
Vestergaard, M. 2004, ApJ, 601, 676
Vestergaard, M., & Osmer, P. S. 2009, ApJ, 699, 800
Vestergaard, M., & Peterson, B. M. 2006, ApJ, 641, 689
Vignali, C., Brandt, W. N., Schneider, D. P., Garmire, G. P., & Kaspi, S. 2003, AJ, 125, 2876
Wang, J.-M., & Zhang, E.-P. 2007, ApJ, 660, 1072
Winter, L. M., Mushotzky, R. F., Reynolds, C. S., & Tueller, J. 2009, ApJ, 690, 1322
Young, M., Elvis, M., & Risaliti, G. 2010, ApJ, 708, 1388
Younger, J. D., et al. 2008, ApJ, 686, 815
Yuan, F. 2007, in ASP Conf. Ser. 373, The Central Engine of Active Galactic Nuclei, ed. L. C. Ho & J.-W. Wang (San Francisco, CA: ASP), 95
Yuan, F., & Narayan, R. 2004, ApJ, 612, 724
Zamojski, M. A., et al. 2007, ApJS, 172, 468